

Journal of Natural Gas Science and Engineering

A quantitative analysis of flow properties and heterogeneity in shale rocks using Computed Tomography imaging and finite-element based simulation

--Manuscript Draft--

Manuscript Number:	
Article Type:	Full Length Article
Keywords:	Unconventional shale rocks; Permeability; Degree of heterogeneity; Eagle Ford; Mancos; Marcellus
Corresponding Author:	James Olugbade Adeleye, Ph.D. First Technical University Rotterdam, NIGERIA
First Author:	James O. Adeleye, Ph.D.
Order of Authors:	James O. Adeleye, Ph.D. Lateef T. Akanji, Ph.D.
Abstract:	<p>A quantitative evaluation of flow property influenced by micro-scale heterogeneities in shale rocks is presented. Micro- and nano-Computed Tomography images of shale rock samples obtained from Mancos, Marcellus and Eagle Ford formations are digitised into entities such as shale grains, organic matter (kerogen), shale minerals, pores and micro-cracks. Numerical computation on selected layers and sub-micron divisions of the geometries is then carried out using a computationally efficient finite-element based simulation algorithms. Parameters such as pore-volume distribution, porosity, permeability and heterogeneity factor within and across layers are computed as part of pre- and post-process operations. The results of these flow properties characterisation indicated that the presence of micro-cracks in the shale samples contributed to the observed wide variation in permeability and porosity. The highest variance in permeability within a layer is of magnitude 5 in Eagle Ford while a magnitude of 2 was computed for Mancos perpendicular. However, magnitudes of 1 and 4 are recorded across layers for Mancos perpendicular and Eagle Ford perpendicular respectively. Contrary to existing assumption that heterogeneity at pore-scale is negligible, it is established from the aforementioned analysis that micro-scale heterogeneity can be quantified. Furthermore, through the analysis of variance and root-mean-square values, it was concluded that tortuosity is inversely related to porosity, permeability and their degree of heterogeneity.</p>
Suggested Reviewers:	Jan Goral, Ph.D jan.goral@utah.edu Lin Ma, Ph.D lin.ma@manchester.ac.uk

Highlights

- Physical and flow properties of shale rock are characterised using digital imaging
- Pore volume distribution in shale shows heterogeneity
- Heterogeneity in shale rock is up to the magnitude of five
- There is variation in permeability both across the layers and rows

1
2
3
4
5
6
7
8
9
10
11
12
13
14
15
16
17
18
19
20
21
22
23
24
25
26
27
28
29
30
31
32
33
34
35
36
37
38
39
40
41
42
43
44
45
46
47
48
49
50
51
52
53
54
55
56
57
58
59
60
61
62
63
64
65

Graphical Abstract

A quantitative analysis of flow properties and heterogeneity in shale rocks using Computed Tomography imaging and finite-element based simulation

James O. Adeleye, Lateef T. Akanji

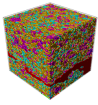
1
2
3
4
5
6
7
8
9
10
11
12
13
14
15
16
17
18
19
20
21
22
23
24
25
26
27
28
29
30
31
32
33
34
35
36
37
38
39
40
41
42
43
44
45
46
47
48
49
50
51
52
53
54
55
56
57
58
59
60
61
62
63
64
65

Highlights

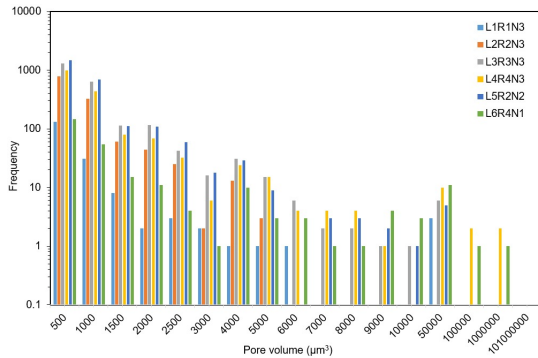
A quantitative analysis of flow properties and heterogeneity in shale rocks using Computed Tomography imaging and finite-element based simulation

James O. Adeleye, Lateef T. Akanji

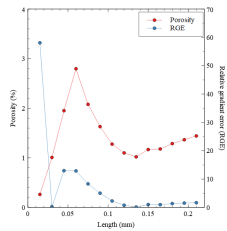
- Physical and flow properties of shale rock are characterised using digital imaging
- Pore volume distribution in shale shows heterogeneity
- Heterogeneity in shale rock is up to the magnitude of five
- There is variation in permeability both across the layers and rows



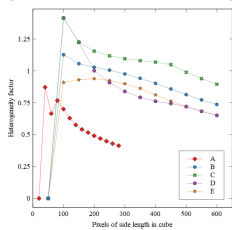
(a) Eagle Ford perpendicular sub-sub-samples selected for simulation showing all the entities (grains, minerals, pores and cracks) extracted in sample L4R2N4.



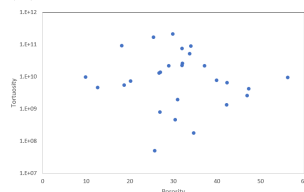
(b) Pore volume distributions showing heterogeneity of Mancos parallel samples L1R1N3, L2R2N3, L3R3N3, L4R4N3, L5R2N2, and L6R4N1.



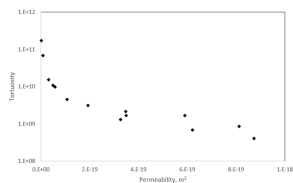
(c) Porosities plot as a function of length scale of the geometries to define REV and their corresponding RGE versus length scale of the geometries used for Eagle Ford parallel nano REV.



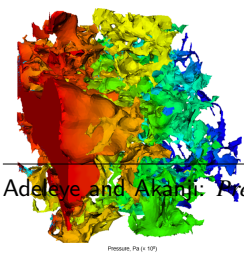
(d) Pore-volume distribution heterogeneity factor and the side length of the digital core for both micro and nano image resolutions. The samples are Eagle Ford parallel nano (A), Mancos parallel (B), Mancos perpendicular (C), Marcellus parallel (D), and Marcellus perpendicular (E).



(e) Tortuosity versus porosity correlation for Mancos perpendicular.



(f) Tortuosity versus permeability correlation for Eagle Ford perpendicular.



A quantitative analysis of flow properties and heterogeneity in shale rocks using Computed Tomography imaging and finite-element based simulation

James O. Adeleye, Lateef T. Akanji

Faculty of Engineering, First Technical University, Nigeria

Petroleum Engineering Division, School of Engineering, University of Aberdeen, Aberdeen, UK

ARTICLE INFO

Keywords:

Unconventional shale rocks
Permeability
Degree of heterogeneity
Eagle Ford
Mancos
Marcellus

ABSTRACT

A quantitative evaluation of flow property influenced by micro-scale heterogeneities in shale rocks is presented. Micro- and nano-Computed Tomography images of shale rock samples obtained from Mancos, Marcellus and Eagle Ford formations are digitised into entities such as shale grains, organic matter (kerogen), shale minerals, pores and micro-cracks. Numerical computation on selected layers and sub-micron divisions of the geometries is then carried out using a computationally efficient finite-element based simulation algorithms. Parameters such as pore-volume distribution, porosity, permeability and heterogeneity factor within and across layers are computed as part of pre- and post-process operations. The results of these flow properties characterisation indicated that the presence of micro-cracks in the shale samples contributed to the observed wide variation in permeability and porosity. The highest variance in permeability within a layer is of magnitude 5 in Eagle Ford while a magnitude of 2 was computed for Mancos perpendicular. However, magnitudes of 1 and 4 are recorded across layers for Mancos perpendicular and Eagle Ford perpendicular respectively. Contrary to existing assumption that heterogeneity at pore-scale is negligible, it is established from the aforementioned analysis that micro-scale heterogeneity can be quantified. Furthermore, through the analysis of variance and root-mean-square values, it was concluded that tortuosity is inversely related to porosity, permeability and their degree of heterogeneity.

1. Introduction


Permeability is required for continuum flow computation and formulation of apparent permeability in shale to account for flux deviation caused by slip flow and Knudsen diffusion (Javadpour, 2009; Kazemi and Ali, 2015). The importance of permeability has led to various proposed models and methods for its estimation. For instance, Javadpour (2009) developed a flux equation by combining slip flow and Knudsen diffusion into gas flux equation to formulate an apparent permeability. Their model was compared to the well-known Darcy's law. Florence et al. (2007); Civan et al. (2012); Sakhaee-Pour and Bryant (2012) used the Hagen-Poiseuille-type equation proposed by Ali Beskok (1999) to develop apparent gas permeability in connection with Knudsen number while Clarkson et al. (2012) introduced their apparent permeability equation with the dynamic slippage concept. Niu et al. (2014) presented a second order gas apparent permeability formulation which revealed that the pore-wall structure of the shale contributed more to the permeability than the property of the gas. Zhang et al. (2015) developed a new method by considering the effect of surface diffusion. Meanwhile, existing methods have estimated intrinsic/ liquid/ Darcy's permeability of shale from conventional theory.

Generally, permeability of porous media depends on pore structure and its relationship with porosity, tortuosity, solid

particle size, pore radius, and specific surface area (Akanji et al., 2013; Akanji and Matthai, 2009; Yang et al., 2017; Ahmadi et al., 2011). The knowledge and understanding of permeability are extremely important for evaluation and development of reservoir (Zheng and Li, 2015; Rezaee, 2015). There exists, therefore, a need for emphasis and critical examination on the nature and the degree of effect of pore structure. For unconventional shale rocks, pore structure is characterised by high pore size-distribution which may translate to permeability heterogeneity (Bhandari et al., 2015; Tinni et al., 2012; Wang et al., 2016; Adeleye and Akanji, 2017). Meanwhile, the displacement of hydrocarbon and flow pattern within porous media is typically influenced by permeability heterogeneity (Djebbar and Donaldson, 1996; Tiwari et al., 2013). Hence, the study of shale permeability is an important step towards understanding of shale heterogeneity and shale flow characterisation.

Permeability anisotropy, mechanical, and acoustic role on shale reservoir characterisation and field development have been investigated and reported in the literature (Tutuncu, 2012); combining Focus Ion Beam Scanning Electron Microscopy (FIB-SEM) and Micro-Computed Tomography (micro-CT) imaging methodologies to investigate the heterogeneity of shale sample (Chen et al., 2013); influence of pore-scale anisotropy and pore distribution on permeability (Tao et al., 2019) and the use of REV to study shale rock heterogeneity (Saraji and Piri, 2015). However, there are no reports on studies of pore-scale permeability heterogeneity from digitised images of core samples obtained from shale rocks. Recent develop-

*Corresponding author

 adeleye.james3@gmail.com (J.O. Adeleye)

ORCID(s):

ments in pore-scale characterisation methods and advanced imaging technologies have enabled the morphological visualisation of the localised grain, clay networks, pore, and kerogen in small shale samples (Tarik et al., 2017; Adeleye and Akanji, 2017; Shabro et al., 2014; Garcia et al., 2009).

The simulation results of small-scale digital cores such as the one obtained from FIB-SEM are not representative due to small volume sizes. Also, the organic pore size of a shale rock is excessively small, so there is need for constructing larger-scale digital cores. Micro-structural characterisation of porous media via imaging has evolved over the past few years. Though advances in computational resources with the imaging capabilities have been useful in direct quantification of porosity, permeability, rock minerals and pore network connectivity (Blunt et al., 2013; Rocha and Cruz, 2010; Akanji and Matthai, 2009; Zhaoli and Zhao, 2002), computational power required for simulating flow through a representative shale sample is enormous and an efficient algorithm solution is yet to be provided.

Further, mineral types and its distributions affect simulation outputs, so does distribution of fluids. Hence, fluid flow simulation through shale rocks becomes more computationally demanding due to diverse and wide distributions of minerals and fluids (Zhu, 2019). Micro and nano-CT are non-destructive imaging techniques developed to acquire information from objects. The operation of the non-destructive machine does not have any impact on the sample being scanned as the sample can still be used for further analysis. In addition, Blunt et al. (2013); Akanji and Matthai (2009) have characterised flow behaviour within the pore-space of sandstone and carbonate rock samples by solving the Stokes equation. All of these provide the requisite background knowledge for studying permeability heterogeneity in shale rocks.

In this work, seven shale rock samples and a total of 588 sub-samples are obtained from Mancos, Marcellus and Eagle Ford formations and scanned using micro and nano-CT imaging technique. The digitised images are then thresholded, segmented and processed to obtain routine rock properties. Navier-Stokes equations are then solved using finite-element method (FEM) and results post-processed to obtain pore volume and porosity distribution and permeability heterogeneity. Going forward, for convenience, we will use the term permeability to refer to liquid/ intrinsic/ Darcy's permeability in this work.

2. Methodology

Micro-and nano-CT experimental scanning of rock samples obtained from Mancos, Marcellus and Eagle Ford formations are carried out. For each formation rock sample (Mancos and Eagle Ford), one micro-CT scanned and 96 sub-samples were obtained, thresholded, segmented and processed. A total of seven samples and 588 sub-samples were characterised. In addition to micro-imaging, a nano-image

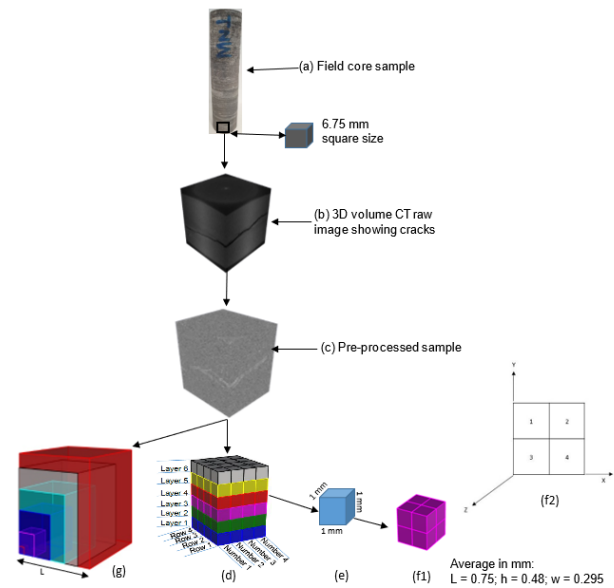


Figure 2: Workflow for the analysis of pore-scale heterogeneity. (a) A typical shale core sample from the field (labelled $MN \perp$ - Mancos perpendicular); (b) 3D reconstruction volume of CT raw image (cracks can be seen on the image); (c) A pre-processed sample for morphological and segmentation; (d) Graphical annotation design for heterogeneity analyses; (e) Sample description used for static heterogeneity analysis; (f1) Different re-cropped samples used for simulation modelled and illustration of their naming convention in (f2). Their average length, height, and width are 0.75 mm, 0.48 mm, and 0.295 mm respectively; (g) Graphical illustration of representative elementary volume (REV) analysis.

of Eagle Ford was obtained and processed sample configured for numerical computation. The spread of variables such as porosity and permeability are then analysed. Selected sub-samples were further sub-divided into sub-micron scale for the purpose of heterogeneity analysis. Figure 2 shows a systematic procedure for accomplishing the aim of this work. The procedure of obtaining data from steps (a) to (e) in Figure 2 have been explained in Adeleye and Akanji (2017). The segmented pores, organic matter, shale grains and mineral components are presented in Figures 3 to 8. Prior to selection of samples for further analysis, the degree of sample heterogeneity was investigated through volume fractions (Tables 11 to 29), pore volume distributions (Figures 9, 10, 11 and 12), REV (Figures 13 to 17), and pore-distribution heterogeneity (Figure 18). Porosity (Tables 11 to 17), organic matter (Tables 18 to 23) and mineral components (Tables 24 to 29) were measured from each segmented components for each of the subcropped samples after processing.

Samples whose pore structure will allow flow are selected and further subcropped into eight (Figures 2(f1) and (f2)). The numbering technique adopted in this study is as shown in Figure 2 (f2). Figure 2 (f2) shows first planar 1, 2, 3 and 4 and the second planar 5, 6, 7, and 8 arranged towards 'Z' direction. In general, the corresponding number on each

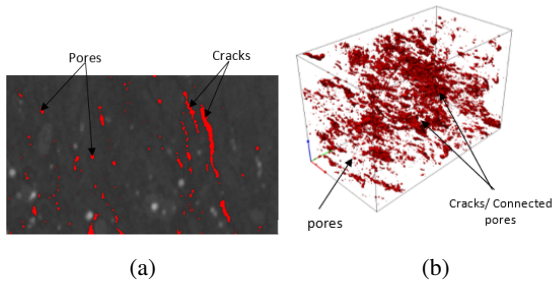


Figure 3: Nano-CT image of Eagle Ford parallel at a resolution of 750 nm and physical extent of 0.2145 mm × 0.393 mm × 0.24975 mm. Showing segmented pores (red) and micro cracks (red) in (a) 2D and (b) 3D.

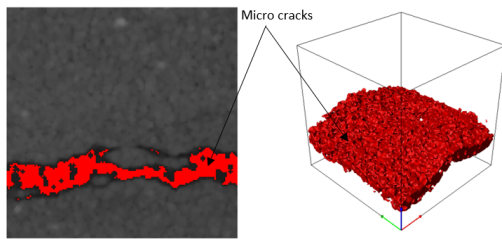


Figure 4: Pore volume (in 3D and 2D red colour) measured for each of the sub-cropped samples after processing.

sample is attached to the parent name (e.g. L3R2N4-4). A typical naming convention such as L3R2N4-4 as adopted in this work means layer 3, row 2, number 4 and sub-number 4. Table 12 showed example of the porosity for sub-cropped sample used for numerical computation. Note that high porosity recorded for L3R2N4-3, L3R2N4-4, L3R2N4-7 and L3R2N4-8 was as a result of re-cropping to accommodate the computation capacity of the system. Hence, the porosity should not be misconstrued as the original porosity of the shale samples used. Figures 3 to 8 show that pore in shale rock are not regular in shapes and their network is complicated.

A stereolithography (STL) file was generated from the processed 3D image volume. After that, organic minerals, shale grains, minerals and pore spaces were extracted from the STL file in a computer aided design (CAD) that uses non-uniform rational B-splines (NURBS). NURBS describes complex 3D surfaces by creating surface meshes within the pore spaces and represent their geometry mathematically. All the samples shown in Figures 5 to 7 were re-cropped (a typical sample is shown in Figure 8) and are meshed (Figure 20 is a typical meshed sample) with the flexibility that the FEM offers to capture the flow geometry (See a typical workflow for FEM in Figure 19) and some results are presented in Figures 31 to 33.

2.1. Characterisation of heterogeneity in shale rocks

It is difficult to estimate petrophysical properties of shale due to its heterogeneity. As a result, measurement of porosity and other properties is challenging. We characterised shale samples to show their degree of heterogeneity. The

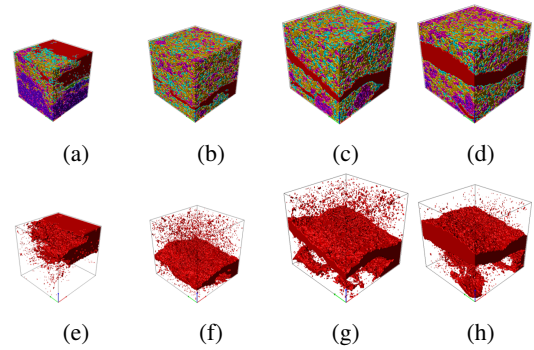


Figure 5: Eagle Ford perpendicular sub-sub-samples selected for simulation showing all the entities extracted in (a) L3R2N4 (b) L4R2N4 (c) L4R3N4 (d) L4R4N4 and pores (e) L3R2N4 (f) L4R2N4 (g) L4R3N4 (h) L4R4N4. || a - d with pores/cracks shown as e - h ||.

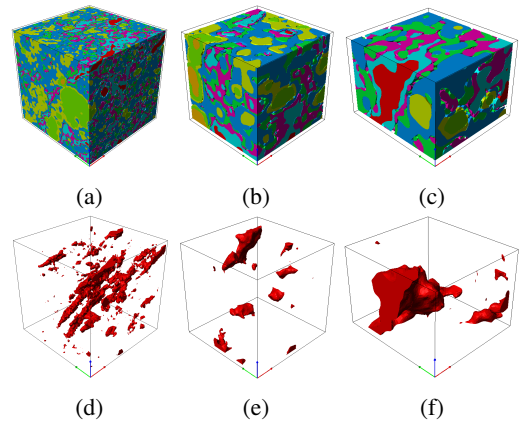


Figure 6: Eagle Ford parallel subsamples from nano resolution selected for simulation. Showing all the entities extracted in (a) L2R3N1 (b) 50N (c) Nano-10 and pores (d) L2R3N1 (e) 50N (f) Nano-10.

effects of volume fractions (VoF) (for porosity, organic matter and minerals), pore volume distributions, REV and pore-distribution are studied to explore their influence on heterogeneity and later related to shale permeability heterogeneity. The volume fractions, pore volume distributions and REV are estimated by adopting the procedure previously published by Adeleye and Akanji (2017) while pore-distribution heterogeneities are estimated by using model (Equation 1) proposed by Wang et al. (2016).

2.1.1. Volume fractions

The computed porosity (in terms of volume fractions) analysed for Eagle Ford perpendicular, Mancos Parallel, Mancos perpendicular, Marcellus Parallel, Marcellus perpendicular and Eagle Ford parallel nano, are between 4.44E-04 (sample L2R1N1) and 1.0 % (sample L6R2N2), 2.1E-03 (sample L2R1N1) and 28.1 % (sample L4R4N4), 8.9E-04 (sample L3R1N1) and 0.61 % (sample L5R3N3), 0 (Several samples) and 9.78 % (sample L4R4N3), 0 (Several samples) and 3.6E-04 % (sample L5R3N3), 3.0E-05 (sample L2R1N1) and 0.12 % (sample L6R3N3) and 0.54 (sample L1R2N1)

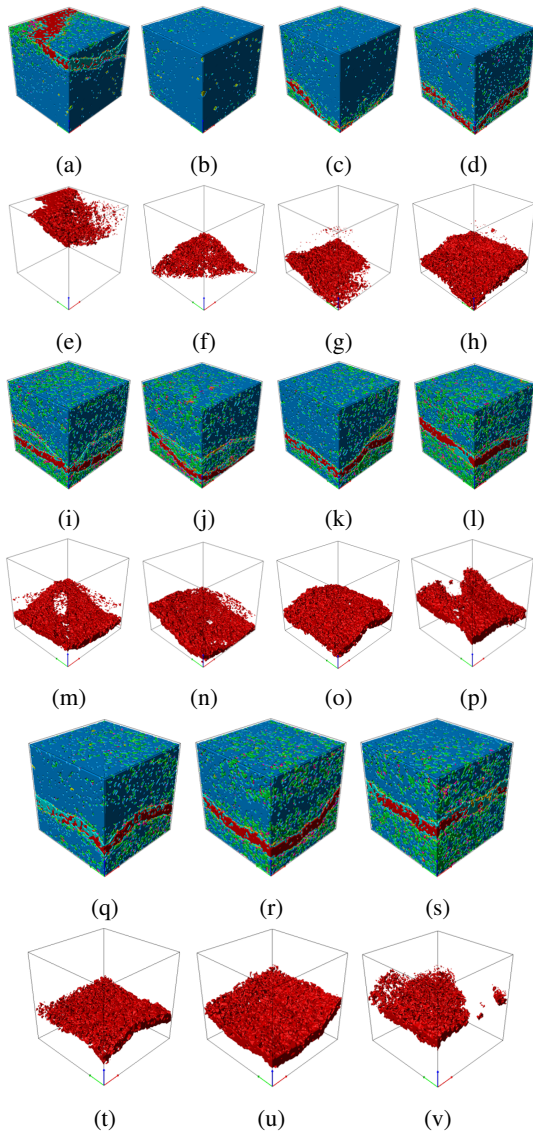


Figure 7: Mancos perpendicular sub-sub-samples selected for simulation showing all the entities extracted in (a) L3R1N4 (b) L4R1N2 (c) L4R2N2 (d) L4R2N2 (i) L4R2N3 (j) L4R2N4 (k) L4R3N2 (l) L4R3N4 (q) L4R4N2 (r) L4R4N3 (s) L4R4N4 and pores (e) L3R1N4 (f) L4R1N2 (g) L4R1N3 (h) L4R2N3 (m) L4R2N4 (n) L4R3N2 (o) L4R3N4 (p) L4R4N2 (u) L4R4N3 (v) L4R1N2. || a - d with pores/cracks shown as e - h; i - e with pores shown in m - p; q - s with pores shown as t - v ||

and 3.86 % (sample L2R3N1) respectively (Tables 11 to 17). These ranges show the extent of statistical dispersion and the variant values of porosity recorded indicated that shale rock is highly heterogeneous in nature. Tables 14, 15 and 16 that Mancos perpendicular, Marcellus parallel and Marcellus perpendicular have the least porous sub-samples as some sub-samples are 0 (see Tables 14, 15). Apart from Eagle Ford perpendicular and Eagle Ford parallel (nano resolution) which are the first two samples with the highest average porosity, Mancos perpendicular is the third-highest average porosity of 0.99 %. This is as a result of the magnitude of cracks which spanned through layer 4 (see Figure 14). On

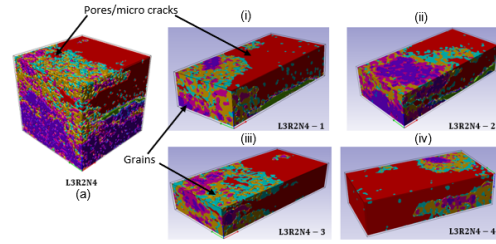
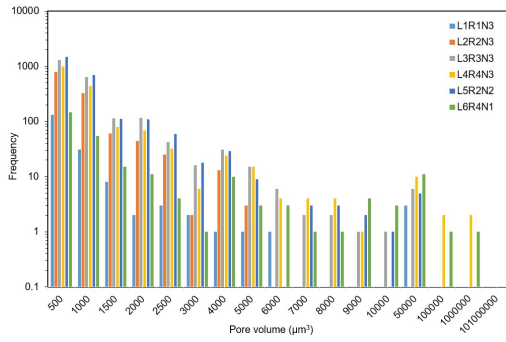


Figure 8: A typical processed sample EGF L3R2N4 (a) cropped into four sections (i - iv). It is showing the sub-number of subcropped

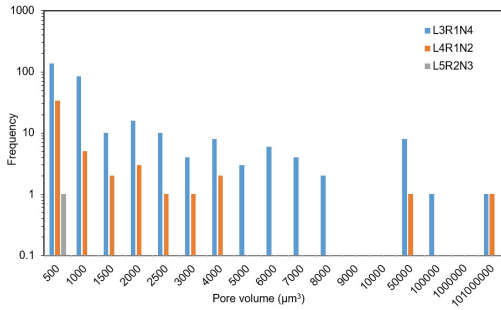
this account, its is obvious to say that heterogeneity exist and is more pronounced at this scale of investigation.

In a similar manner, the volume fraction of organic matter and mineral is shown in Tables 18 to 29. The distribution variants of their volume fraction did not only contribute to the heterogeneity of shale rock but further confirmed it. The volume fraction of organic matter (Tables 18 to 23) was correlated with measured TOC from published organic matter. For Eagle Ford sample, the range of imaging results was 8.4E-3 to 25.3 % compared with TOC ranges of Alqahtani and Tutuncu (2014), Murphy et al. (2013), Zhang et al. (2016) and Mullen (2010); Curtis et al. (2012); Jennings and Antia (2013); Eker et al. (2014) who reported 2.7 to 7.64 %, 0.57 to 14.2 %, 2.1 to 5.7 % and 0.03 to 10.5 % respectively. For the Mancos sample, the range of imaging results was 3E-5 to 12 % compared with Torsaeter et al. (2012), Ridgley et al. (2013) and Zhang et al. (2016) who reported TOC ranges of 1 to 1.27 %, 0.4 to 3.1 % and 0.82 to 1.36 % respectively. For Marcellus, the range of imaging results was 1.2E-3 to 7.0 % compared with Milici and Swezey (2006), Bruner and Smosna (2011) and Belvalkar and Oyewole (2010) who reported TOC ranges of 1.4 to 4.3 %, 2 to 10 % and 3 to 6 % respectively.

The VoF of minerals in Tables 24 to 29 (which is assumed to be pyrite) in this work was correlated with published X-ray powder diffraction (XRD) shale data. Comparatively, the range of VoF of the pyrite from imaging technique in this work is 6.1E-3 to 6.9 % while Mullen (2010); Morsy et al. (2013); Jennings and Antia (2013); Alqahtani and Tutuncu (2014) reported 1.3 to 5 % range for Eagle Ford. For Mancos, the range of VoF of the pyrite is 1.3E-2 to 0.97 % while 2 % was reported by Torsaeter et al. (2012). For Marcellus, the range of VoF of the pyrite is 5.6E-4 to 1.2 % and 3.18 to 13 % for Bruner and Smosna (2011); Gupta and Mishra (2017). The slight difference between the results is due to the fact that pyrite is a parent rock which may be sparsely distributed. Further, the samples were taken from different locations. The contribution of this mineral to the heterogeneity of shale rock can also be underlined.

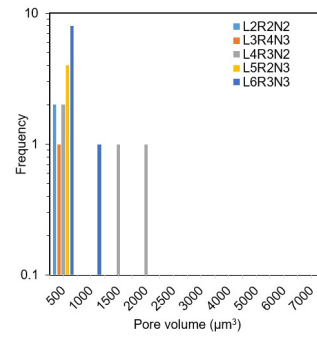


(a)

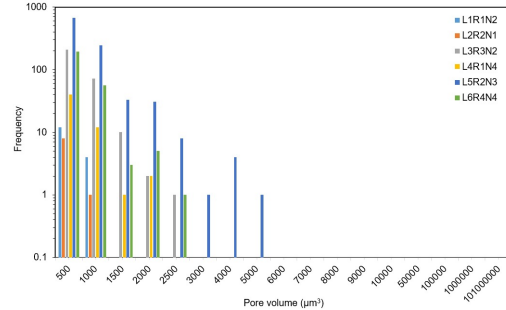


(b)

Figure 9: Pore volume distributions showing heterogeneity (a) Mancos parallel (L1R1N3, L2R2N3, L3R3N3, L4R4N3, L5R2N2, and L6R4N1) (b) perpendicular (L3R1N4, L4R1N2, and L5R2N3) samples.



(a)



(b)

Figure 10: Pore volume distributions showing heterogeneity (a) Marcellus parallel (L2R2N2, L3R4N3, L4R3N2, L5R3N2, and L6R3N3) (b) perpendicular (L1R1N2, L2R2N1, L3R3N2, L4R1N4, L5R2N3, and L6R4N4) samples.

2.1.2. Pore-volume distribution (PVD)

The effect of PVD heterogeneity on shale rock permeability heterogeneity is evaluated in this section. The marching cube algorithm is used to obtain pore volume of selected sub samples (See Adeleye and Akanji (2017)). The pore-volume are formed into classes and the upper limits of each class is plotted against the frequency. The results for each shale rock sample is presented thus:

- PVD for Mancos:

Figure 9 shows the PVD of selected Mancos parallel and perpendicular samples at micro-scale resolution. By their nature, a wider range of pore volume is observed in both sets of samples. For instance, the frequencies of the $500 \mu\text{m}^3$ pore volumes for samples L5R2N2 and L3R1N4 are 58.9 % and 46.4 % respectively. Pore volume varied appreciably across the layers. Although, both parallel and perpendicular samples have similar PVD patterns, there is a significant difference within Mancos perpendicular samples. This is as a result of the relatively less or no pore volume captured in layer one, two, five and six. In addition, layers three and four have scanty and dispersed pore volume.

- PVD for Marcellus:

Figure 10 provides the PVD of selected Marcellus parallel and perpendicular samples at micro resolution. Marcellus subsamples, appears to have limited range and low frequency of pore volume than Mancos and

Eagle Ford. In the Marcellus perpendicular, the distribution spreads out much to the right than in the Marcellus parallel, although pore volume still varied appreciably across the layers (Figure 10). There are 50 % and 67.6 % frequencies of the pore volume in the range of $500 \mu\text{m}^3$ for Marcellus parallel (L4R3N2) and Marcellus perpendicular (L5R2N3) samples respectively, while the largest pore volume in the range of $2000 \mu\text{m}^3$ and $5000 \mu\text{m}^3$ for Marcellus parallel (L4R3N2) and Marcellus perpendicular (L5R2N3) have 25 % and 0.1 % frequencies respectively.

- PVD for Eagle Ford:

Figures 11 provide the PVD of selected Eagle Ford parallel and perpendicular samples at micro resolution while Figure 12 provides PVD of selected Eagle Ford perpendicular samples at nano resolution. In comparison, both parallel and perpendicular samples have similar PVD patterns. By their nature, a wider range of pore volumes is observed in Figures 11 and 12 and the amount differs significantly across the sub-samples. For instance, there are 59.6 % and 47.9 % frequencies of the pore volume in the range of $500 \mu\text{m}^3$ for Eagle Ford parallel (L6R3N3) and Eagle Ford perpendicular (L6R4N4) samples respectively while Eagle Ford parallel (L2R3N1) nano resolution has 79% frequency of the pore volume in the range of $2 \mu\text{m}^3$. Meanwhile, the largest pore volume in the range of $1\text{E}6 \mu\text{m}^3$, $1\text{E}5 \mu\text{m}^3$ and $2\text{E}4 \mu\text{m}^3$ for Eagle Ford par-

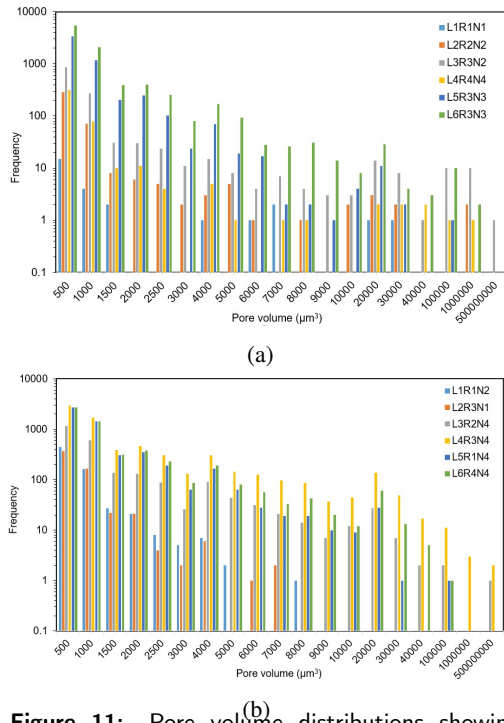


Figure 11: Pore volume distributions showing heterogeneity (a) Eagle Ford parallel (L1R1N1, L2R2N2, L3R3N2, L4R4N4, L5R3N3, and L6R3N3) (b) perpendicular (L1R1N2, L2R3N1, L3R2N4, L4R3N4, L5R1N4, and L6R4N4) samples.

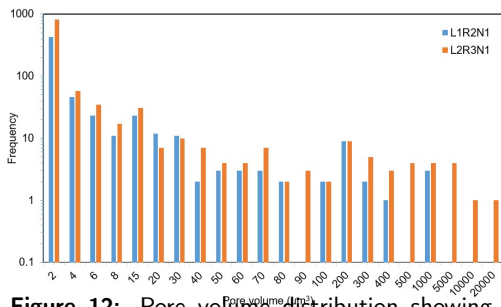


Figure 12: Pore volume distribution showing heterogeneity of Eagle Ford perpendicular samples (L1R2N1 and L2R3N1) at nano resolution.

allel (L6R3N3), Eagle Ford perpendicular (L6R4N4) and Eagle Ford parallel (L2R3N1) nano resolution have 0.02 %, 0.017 % and 0.09 % frequencies respectively. Pore volume varied appreciably across the layers (Figures 11 and 12). By way of illustration, layer one to six of Eagle Ford parallel has frequency between 55.6 % and 72.3 % of the pore volume in the range of 500 μm^3 while Eagle Ford perpendicular has frequency between 42.2 % and 65.6 %. Evidently, this was observed in nano resolution sample (Eagle Ford parallel-L2R3N1) too as the difference between the two layers was 6 % of the pore volume in the range of 2 μm^3 .

Generally, the distribution results indicate that pores are split unevenly between smaller and larger ones. However, contributions of smaller pores to heterogeneity is insignifi-

cant compared to larger pores. Smaller pore volumes have a higher frequency while bigger pore volumes have a lower frequency, though with substantial percentages of total pore volume. Despite the fact that the frequency of small pore volume is high, we knew they are still underestimated as more are still below the resolution of the image used in this work. This is depicted by their positively skewed PVD Figures. We selected few samples with requisite pore features for fluid flow simulation (see sections 2.2.1 and 2.2.4).

2.1.3. Representative elementary volume (REV)

To obtain a reliable REV, porosity plots were constructed at different physical length using an interval of 0.34 mm to 4.05 mm; resulting in a 12 data points. Figures 13 to 17 show relative gradient error (RGE) and porosity plotted against length scale for Mancos parallel 2, Mancos perpendicular, Marcellus parallel 2, Marcellus perpendicular 2, Eagle Ford parallel 3 nano samples respectively. Similar plots were generated for higher resolution sample at different physical length using an interval of 0.015 mm to 0.21 mm which gives 14 data points (Figure 17). It can be seen from Figures 13 to 17 that spatial distribution of porosity is influenced by high heterogeneity nature of shale which has been discussed earlier. The corner point reference technique was used to plot Figures 13 to 17.

It was observed that small incremental growth in sub-cropped samples produces random variation in porosity that show the domain of microscopic effects of shale (Figures 13, 15 and 16). At larger physical length between 2.36 mm and 4.05 mm porosity, show the characteristics of porous medium domain except for Mancos parallel 2 and Mancos perpendicular samples. Conversely, ϵ_g keeps decreasing below the criterion of 0.5 REV with increasing sub cropped volume. In Figure 14, the observed difference in behaviour is due to the linearity of porosity variation which is insignificant at minimal incremental growth; then there is gradual porosity increase until 3.04 mm and afterwards increased sharply. The sharp increase was as well noticed at different length in all the samples. While characteristics of porous medium was not evident in Mancos parallel 2 and Mancos perpendicular samples, the increase of porosity after 3 mm in Figures 15 and 16 reveal the beginning of in-homogeneous medium region.

Similarly, for Eagle Ford parallel nano resolution sample in Figure 17, there is random variation in porosity for small incremental growth in sub cropped sample. This observation is consistent with domain of microscopic effects of shale. Larger physical length between 0.105 mm and 0.21 mm porosity, show the characteristics of porous medium domain. Unlike the other samples, the effect of the magnitude of change in porosity as sub cropped volume increases reflected on the stability of ϵ_g . Using a criterion of 0.5 to estimate porosity REV, the sample size required will be 1.01 mm (1010 μm) for Marcellus perpendicular and 0.12 mm (120 μm) for Eagle Ford parallel (at 750 nm) respectively. These

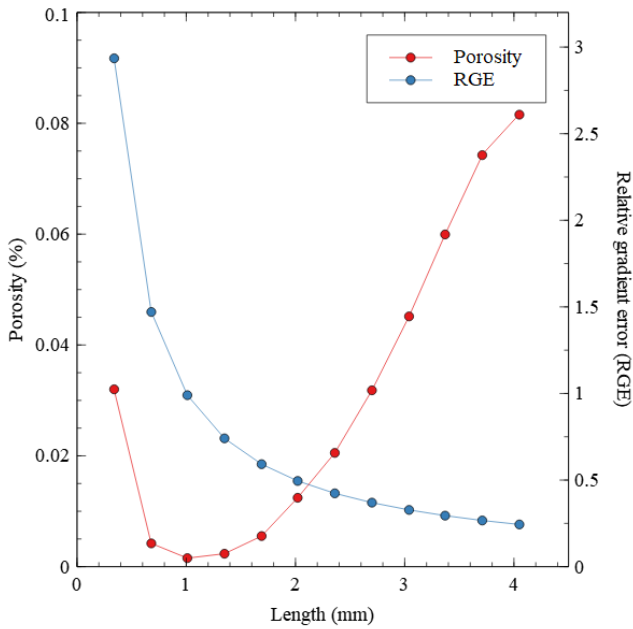


Figure 13: Porosities plot as a function of length scale of the geometries to define REV and their corresponding RGE versus length scale of the geometries used for Mancos parallel REV.

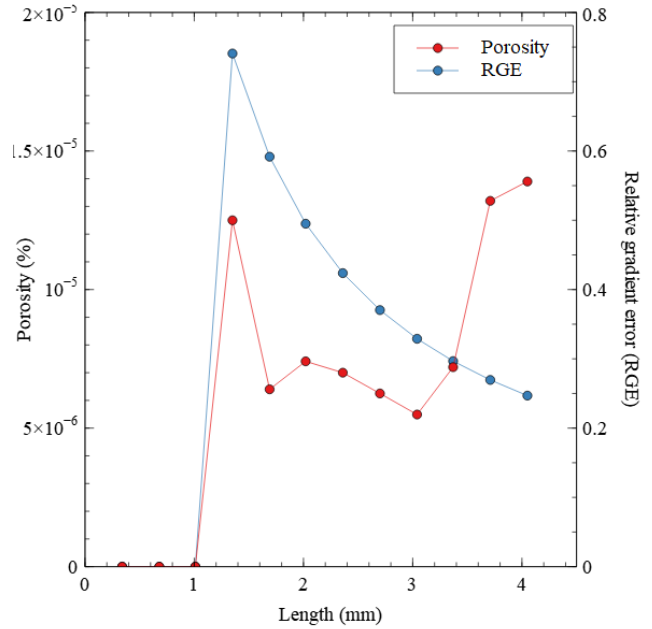


Figure 15: Porosities plot as a function of length scale of the geometries to define REV and their corresponding RGE versus length scale of the geometries used for Marcellus parallel REV.

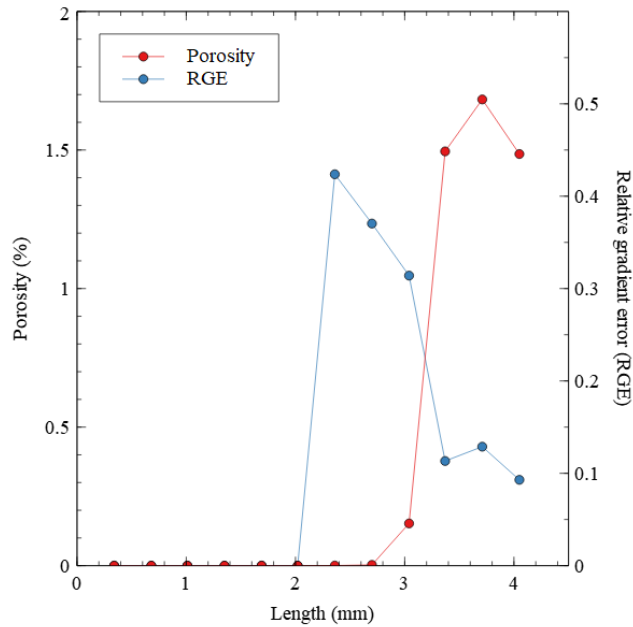


Figure 14: Porosities plot as a function of length scale of the geometries to define REV and their corresponding RGE versus length scale of the geometries used for Mancos perpendicular REV.

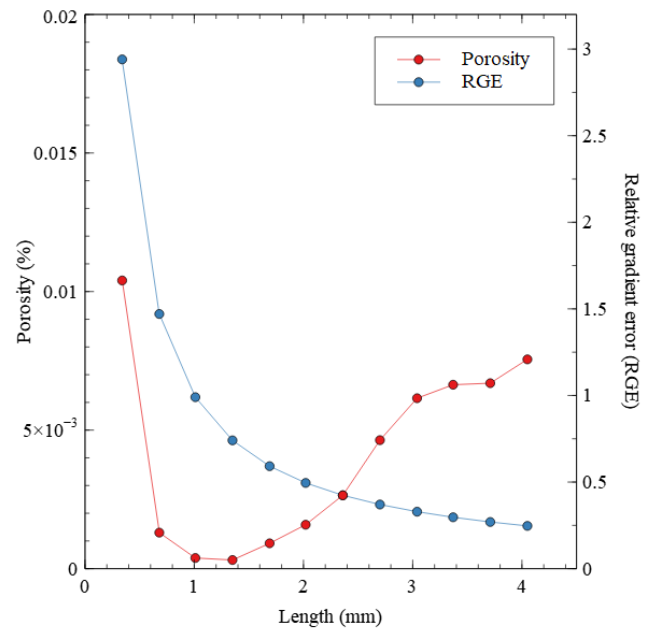


Figure 16: Porosities plot as a function of length scale of the geometries to define REV and their corresponding RGE versus length scale of the geometries used for Marcellus perpendicular REV.

findings reveal that shale rocks do not have stable plateau or distinct domain of porous medium, hence their heterogeneous and complex in nature. Comparing our results with REV results of Bowland shale presented by Ma et al. (2016) to be between 9 and 38 μm , one could see that spatial resolution is key.

The porosity data used for the computation of REV was

adopted for computation of pore-distribution heterogeneity factor (H_{pd}). As proposed by Wang et al. (2016) in equation 1 where H_{pd} is pore-distribution heterogeneity factor, dimensionless; n is number of box from each porous media box; i is sequence number of box; ϕ is the porosity of porous media box, % and ϕ_i is the porosity of the ith porous media

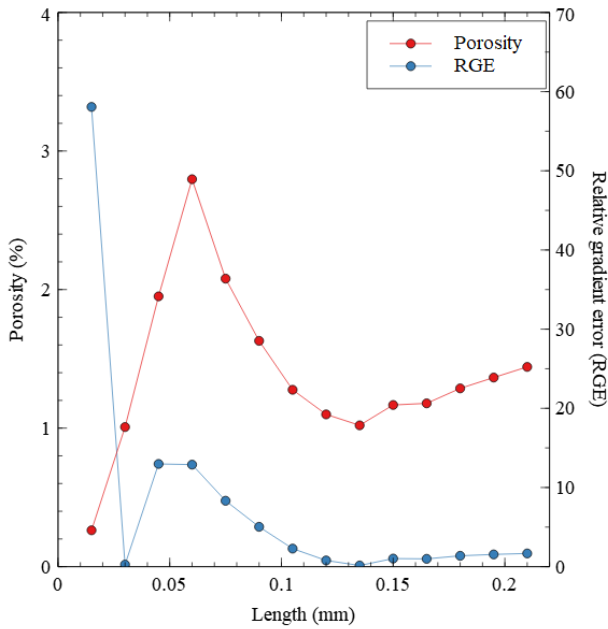


Figure 17: Porosities plot as a function of length scale of the geometries to define REV and their corresponding RGE versus length scale of the geometries used for Eagle Ford parallel nano REV.

box, %. The H_{pd} is the strength of pore-distribution heterogeneity which is expressed as the relative standard deviation of porosity of a porous media box. From Figure 18, the heterogeneity of the shale micro image resolutions (Mancos parallel, Mancos perpendicular, Marcellus parallel, Marcellus perpendicular) show tendency to be stable between 0.7 and 1.2 though slightly deviated starting from the side length of 150 pixels while that of nano image resolutions (Eagle Ford parallel nano) is at 0.57 at side length of 130 pixels. As the strength of stability is not strong enough for both micro and nano resolution show that heterogeneity in shale cut across every scale. The observed heterogeneity factors complement our observations from REV plots.

$$H_{pd} = \frac{1}{\phi} \sqrt{\frac{\sum(\phi_i - \phi)^2}{n - 1}} \quad (1)$$

2.2. Finite-element based simulation approach

A FEM algorithm for NSE in porous media is adopted in this work. The discretised equation is solved using an efficient Algebraic MultiGrid Solver (SAMG) solver library (Stüben, 2001). The work flow for the numerical basis to this mathematical partial differential equations governing the fluid flow at the pore scale is as follows: (i) processing the digitised shale core samples, (ii) meshing the sub-cropped samples with unstructured mesh consisting of triangles and tetrahedron elements, (iii) discretising the flow equation, (iv) material properties, setting boundary, and initial conditions are assigned with Interrelations subclass to solve the discretised equations using algebraic multigrid solver. The computation

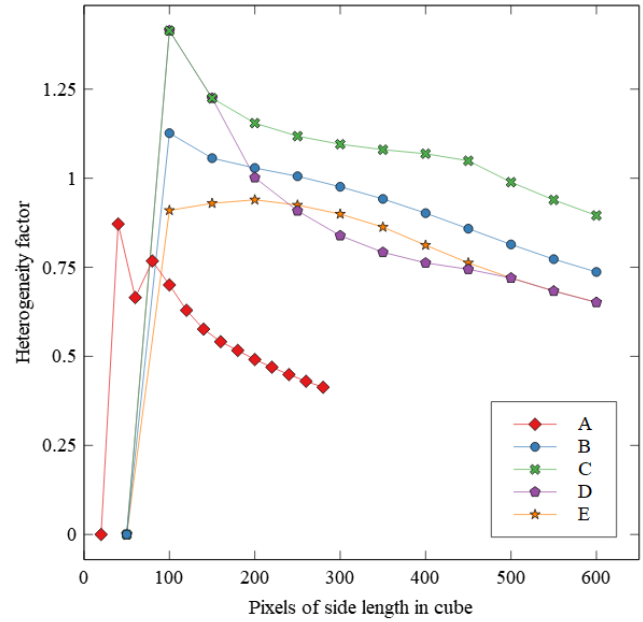


Figure 18: Pore-volume distribution heterogeneity factor and the side length of the digital core for both micro and nano image resolutions. The samples are Eagle Ford parallel nano (A), Mancos parallel (B), Mancos perpendicular (C), Marcellus parallel (D), and Marcellus perpendicular (E).

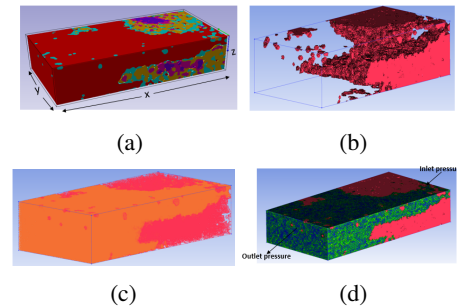


Figure 19: A typical workflow for Eagle Ford perpendicular re-cropped sub-subsample L3R2N4-4 (a) a re-cropped model (b) micro cracks with surface mesh (c) volume mesh skeleton in the CAD, and (d) its full FEM model.

of variable coefficients is done in CSMP ++ platform. (v) visualising and post processing results. This solution work flow approach is shown in Figures 19 and 22. A recent paper by Akanji and Chidamoio (2020) used this algorithm to study oil and gas flow through pipes of different diameters. They did a comprehensive investigation of the workflow computational errors which will not be repeated here. In a nutshell, the process for porosity and permeability computation involves selection of sub-samples, re-cropping and meshing the micro-cracks, pores and geometric surfaces.

2.2.1. FEM discretisation of shale model: Meshing

The shale models are discretised using unstructured grids because they can track free-form geometrical entities like NURBS employed in this work. The surface comprises of

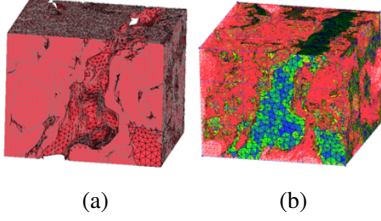


Figure 20: Finite element model of nano-10 sub-sample from Eagle Ford parallel (a) surface (b) volume mesh.

Table 1

Total elements and nodes for Eagle Ford perpendicular samples.

Name	Dimension (mm)	Total elements	Total nodes
L3R2N4-3	1.01 × 0.51 × 0.24	2,437,899	454,835
L3R2N4-4	1.01 × 0.51 × 0.25	1,164,390	222,810
L3R2N4-7	1.01 × 0.49 × 0.24	1,482,099	291,625
L3R2N4-8	1.01 × 0.49 × 0.25	1,431,763	278,699
L4R2N4-4	1.01 × 0.51 × 0.24	6,614,581	1,140,893
L4R2N4-7	1.01 × 0.49 × 0.26	1,792,030	348,424
L4R2N4-8	1.01 × 0.49 × 0.24	2,686,742	503,815
L4R3N4-1	1.01 × 0.51 × 0.25	4,911,153	911,761
L4R3N4-2	1.01 × 0.51 × 0.24	1,501,663	287,435
L4R3N4-6	1.01 × 0.49 × 0.24	3,606,521	679,402
L4R3N4-7	1.01 × 0.49 × 0.25	564,351	106,579
L4R4N4-3	1.01 × 0.51 × 0.24	2,117,412	399,468
L4R4N4-6	1.01 × 0.49 × 0.25	2,498,651	473,203
L4R4N4-7	1.01 × 0.49 × 0.24	4,827,393	853,221

Table 2

Total elements and nodes for Eagle Ford nano resolution samples.

Name	Dimension (mm)	Total elements	Total nodes
L2R3N1-6	0.11 × 0.05 × 0.04	3,272,889	622,597
50N	0.04 × 0.04 × 0.04	3,621,979	669,405
Nano-10	0.03 × 0.03 × 0.02	806,983	158,422

triangles and/or quadrilaterals while pore spaces (volumetric) consist of tetrahedral and/or hexahedra. For this hybrid meshes we ensured the quality of the resulting mesh by keeping the element to node ratio close to two. The unstructured grid (Figure 20 - a typical example of surface mesh) was constructed with spatially variable adaptive refinement to keep the grain boundaries intact and also to capture the tight pore regions. This was achieved by setting the minimum and/ or maximum element size, aspect ratio, skewness. The total number of elements and nodes in the geometric models are in the range of 806,983 to 8,270,775 and 106,579 to 1,574,335 respectively (see Tables 1 to 3). Multiples edges, over-lapping elements, triangle boxes, non-manifold and gaps are factors that lower mesh quality includes. However, qualities of the mesh are improved by high-level diagnostic smoothening and modification algorithm in Integrated Computer Engineering and Manufacturing (ICEM) meshing tool.

2.2.2. Mathematical model

Our focus is to compute intrinsic permeability or liquid permeability which is needed for apparent permeability or gas permeability. For this reason, we assume water as

Table 3

Total elements and nodes for Mancos perpendicular samples.

Name	Dimension (mm)	Total elements	Total nodes
L3R1N4-1	1.01 × 0.51 × 0.39	3,515,965	648,716
L3R1N4-2	1.01 × 0.49 × 0.34	1,393,791	291,932
L4R1N2-2	1.01 × 0.49 × 0.30	2,975,388	556,671
L4R1N3-1	1.01 × 0.51 × 0.24	2,514,935	527,803
L4R1N3-2	1.01 × 0.49 × 0.33	2,284,693	469,884
L4R2N2-1	0.51 × 0.51 × 0.31	2,309,663	470,593
L4R2N2-2	0.51 × 0.49 × 0.34	1,542,930	311,828
L4R2N2-3	0.49 × 0.51 × 0.35	1,549,945	313,680
L4R2N2-4	0.49 × 0.49 × 0.30	2,931,050	588,868
L4R2N3-1	0.51 × 0.51 × 0.42	1,822,406	386,099
L4R2N3-2	0.49 × 0.51 × 0.42	3,984,381	811,856
L4R2N3-3	0.51 × 0.49 × 0.40	2,591,904	491,077
L4R2N3-4	0.49 × 0.49 × 0.37	2,507,074	520,768
L4R2N4-1	1.01 × 1.01 × 0.42	8,270,775	959,918
L4R3N2-1	0.51 × 0.51 × 0.30	3,074,108	1,574,335
L4R3N2-2	0.51 × 0.51 × 0.39	3,239,515	609,225
L4R3N2-3	0.51 × 0.51 × 0.28	4,505,870	642,357
L4R3N2-4	0.51 × 0.51 × 0.32	3,053,843	863,895
L4R3N4-1	0.51 × 0.51 × 0.30	2,470,782	550,688
L4R3N4-2	0.49 × 0.51 × 0.37	2,212,597	413,430
L4R3N4-3	0.51 × 0.49 × 0.32	2,975,750	503,505
L4R3N4-4	0.49 × 0.49 × 0.42	2,028,921	945,345
L4R4N2-1	1.01 × 0.51 × 0.31	2,484,075	619,637
L4R4N2-2	1.01 × 0.49 × 0.26	4,828,087	487,576
L4R4N3-1	0.51 × 0.51 × 0.33	1,788,270	441,565
L4R4N4-1	1.01 × 0.51 × 0.35	5,434,379	366,055
L4R4N4-2	1.01 × 0.4992 × 0.37	5,242,995	971,650

the fluid flowing within the pore network and hence there is no gas adsorption. The Navier-Stokes equations (NSE) is the numerical computation technique adopted for direct flow simulation on images in this work. NSE (Equation 2) which describes the flow of fluids in porous media will not be derived here. Interested reader is referred to standard textbooks such as Pritchard and Leylegian (2010) and Anderson Jr et al. (2009). The equation of motion for an incompressible Navier-Stokes equation can be written as:

$$\rho \frac{\partial \mathbf{u}}{\partial t} + \rho (\mathbf{u} \cdot \nabla \mathbf{u}) - \mu \nabla^2 \mathbf{u} + \nabla P = 0, \quad (2)$$

and the continuity equation as

$$\nabla \cdot \mathbf{u} = 0, \quad (3)$$

where, μ is viscosity, ρ is density, \mathbf{u} is the velocity and $P = p + \rho gh$ is the pressure of the fluid. In Equation 2 the first, second, third, fourth and fifth term are unsteady acceleration, advection, diffusion, pressure and gravitational acceleration terms respectively. No-slip and no fluid penetration conditions are imposed at the boundary between the fluid and the solid by simply setting the velocity at the grain to zero.

$$P = p + \rho gh, \quad (4)$$

where, h is the distance measured in the opposite direction to gravity (Akanji and Matthai, 2009). To enforce the incompressibility, fluid density is assumed to be constant. This means that velocity will not change at any fixed point

in space. Steady-state flow is the focus of this study; hence, the first term will be dropped then Equation 2 becomes:

$$\frac{\mu}{\rho} \nabla^2 \mathbf{u} - \mathbf{u} \cdot \nabla \mathbf{u} = \frac{1}{\rho} \nabla P. \quad (5)$$

Our interest is to solve the full NSE (Equation 5) due to the complex nature of the shale samples which dictates that the convective term be included in the solution sequence. In addition, as flow in shale occur through constricted pores and cracks aperture, we tend to agree with Brush and Thomson (2003), that inertial forces significantly influence the flow field by resisting changes in magnitude and direction. This is as a result of vectors in the large aperture region recirculating due to separation in the flow field. Hence, convective acceleration component is considered other than the regime of flow. We arrived at Stokes equation (Equation 6) when convective term is dropped.

$$\frac{\mu}{\rho} \nabla^2 \mathbf{u} = \frac{1}{\rho} \nabla P. \quad (6)$$

2.2.3. FEM discretisation of mathematical equation

A sequential solution approach is adopted in this study. First, the Stokes equation (Equation 6) is solved and then the results used as a preconditioner to solve for steady state Navier-Stokes Equation 5. Basically, Equation 5 is decoupled thus

$$\mathbf{u} \cdot \nabla \mathbf{u} = f, \quad (7)$$

where f is the Stokes equation (Equation 6).

If it is assumed that pore velocity solved from steady Stokes equation is

$$\mathbf{u} = \psi \nabla P, \quad (8)$$

where ψ is function of the coordinates x , y and z . Velocity obtained from Equation 8 is substituted into Equation 6 to first solve for pressure field.

Equation 8 is substituted into 6 and can be written as

$$\frac{\mu}{\rho} \nabla^2 (\psi \nabla P) - \frac{1}{\rho} \nabla P = f. \quad (9)$$

Substituting Equation 9 back into Equation 7 results in

$$\mathbf{u}_0 \cdot \nabla \mathbf{u} = \frac{\mu}{\rho} \nabla^2 (\psi \nabla P) - \frac{1}{\rho} \nabla P, \quad (10)$$

where u_0 is the initial/trial condition velocity obtained from Stokes equation. The summary of the solution sequence is shown in Figure 22

For the purpose of integration, Galerkin method of discretisation is employed as it is most widely used and applicable. Galerkin makes use of interpolation functions. Interested reader can see the following publications Akanji and

Matthai (2009), Garcia et al. (2009), Smith et al. (2013) and Akanji and Chidamoio (2020). The discretisation of the above partial differential equations are made ready in the PDE operator as described in Garcia et al. (2009) and shown in Figure 22.

2.2.4. Numerical application

For each finite element, the resulting volume integral terms are assembled into a linear algebraic equations of the forms

$$[K] \{P\} = \{q\}, \quad (11)$$

where, K is the global conductance matrix that contains millions of finite-elements nodes, P is the solution vector which holds the nodal fluid-pressure values and q is the source terms and boundary conditions. The pressure is solved first and then velocity u is post processed according to Akanji and Matthai (2009). Subsequently, intrinsic permeability which is the measurement of ease at which a particular fluid flow through a porous media is computed thus:

$$K = \frac{u\mu}{\nabla P}. \quad (12)$$

where ∇P is the pressure difference per unit length along the direction of the main flow, μ is the viscosity, v is the velocity flow rate.

Four no-flow and two Dirichlet boundary conditions are assigned for all 3D simulations (Figure 21). Also, the flow is driven by a pressure difference (ΔP) between the inlet (left) and outlet (right) boundaries of the computational domain and no-flow boundaries are imposed on the remaining sides. The pressure level at the outlet boundary was set to 1×10^5 Pa for all simulations and set to 1×10^5 Pa + dP (where dP for each simulation is given in Tables 4 to 6) at the inlet boundary. The initial permeability and porosity are 1×10^{-12} m² and 0.25 respectively while fluid volume source, viscosity and density are 0.0, 0.001 Pa.s and 1000 kg/m³ respectively.

The volumetric mesh generated in the ICEM is the FEM model used in the numerical simulation (Figure 19). The results demonstrated through this technique show that there is significant computational time savings. The efficiency of the technique adopted in this work relies on the flexibility, speed, stability and accuracy of the solution approach. Owing to its computational capability, it plays an essential role as a simulation tool for a considerable sample size that could still be used for further analysis.

To check if non-Darcy flow exists, we computed Reynolds number as $Re = \rho DU / \mu$ using pore diameters, D (6.75 μ m for micro resolution and 0.75 μ m for nano resolution) of the smallest pores where velocity U rate is expected to be the highest. The results, $1.7E-07 \leq Re \leq 3.8E-03$, are less than 1 and implied that we have laminar flow in all our samples and computation of flow permeability using Darcy's equation is appropriate. The computation of permeability is therefore based on Equation 12. Further, attempts were also made to

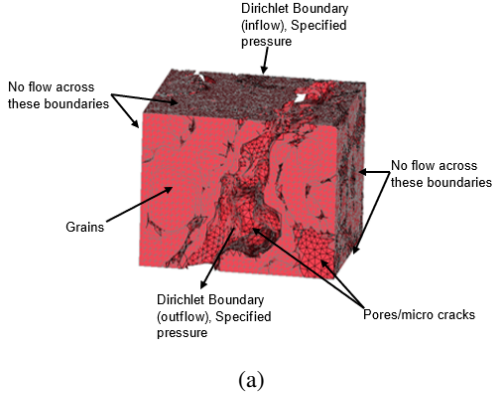


Figure 21: A geometric representation of the model set-up showing boundary conditions with four no-flow and two Dirichlet (inflow and outflow) boundaries.

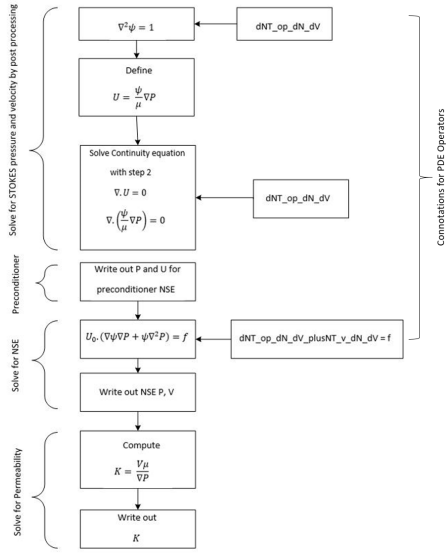


Figure 22: A workflow showing the solution approach adopted in this work. The acronyms to the right are connotations of the partial differential equation (PDE) that emanated from the discretisation of both SE and NSE equations.

verify the relationship between our data and the non-Darcy equation. The Forchheimer Equation as presented by Zhengwen and Reid (2006) thus

$$\frac{dP}{dx} = \frac{\mu v}{K} + \beta \rho v^2. \quad (13)$$

can be rewritten in the form of straight line equation as:

$$\frac{1}{\mu v} \left(\frac{dP}{dx} \right) = \frac{1}{K} + \beta \left(\frac{\rho v}{\mu} \right). \quad (14)$$

where $\frac{1}{\mu v} \left(\frac{dP}{dx} \right)$ is y; $1/K$ (inverse of permeability) is the intercept; β (non-Darcy coefficient) is the slope and $\frac{\rho v}{\mu}$ is x. Here both permeability and non-Darcy coefficient are expected to be positive. For the purpose of this experiment,

Table 4

Maximum velocity obtained for Eagle Ford perpendicular samples.

Name	dP (Pa)	Max velocity (m/s)	No of iterations
L3R2N4-3	30.7	1.66E-06	30
L3R2N4-4	30.7	1.02E-06	29
L3R2N4-7	30.7	1.08E-06	30
L3R2N4-8	80.7	1.29E-06	27
L4R2N4-4	30.7	4.26E-06	23
L4R2N4-7	30.7	1.42E-06	30
L4R2N4-8	40.7	1.21E-06	30
L4R3N4-1	40.7	1.78E-06	30
L4R3N4-2	189.7	2.74E-06	26
L4R3N4-6	89.7	3.18E-06	30
L4R3N4-7	89.7	1.06E-06	17
L4R4N4-3	90.7	1.00E-06	30
L4R4N4-6	89.7	2.90E-06	30
L4R4N4-7	89.7	2.75E-06	29

Table 5

Maximum velocity obtained for Eagle Ford nano resolution samples.

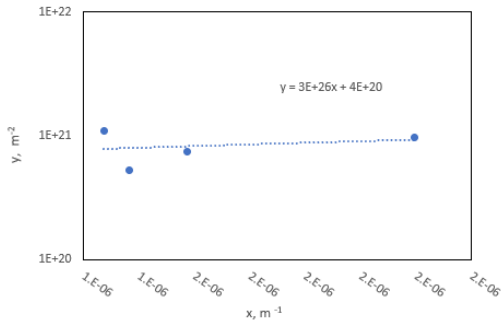
Name	dP (Pa)	Max velocity (m/s)	No of iterations
L2R3N1-6	38	5.1E-03	30
50N	0.45	4.01E-07	30
Nano-10	0.40	2.33E-07	22

Table 6

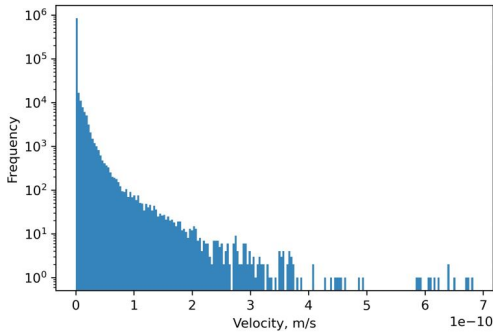
Maximum velocity obtained for Mancos perpendicular samples.

Name	dP (Pa)	Max velocity (m/s)	No of iterations
L3R1N4-1	19.8	1.42E-06	30
L3R1N4-2	39.8	1.03E-06	30
L4R1N2-2	39.8	1.15E-06	30
L4R1N3-1	79.8	1.09E-06	30
L4R1N3-2	199.8	1.69E-06	30
L4R2N2-1	69.8	2.22E-06	30
L4R2N2-2	69.8	1.53E-06	30
L4R2N2-3	69.8	2.62E-06	22
L4R2N2-4	39.8	1.10E-06	30
L4R2N3-1	39.8	1.96E-06	30
L4R2N3-2	39.8	2.63E-06	30
L4R2N3-3	39.8	3.23E-06	30
L4R2N3-4	39.8	4.61E-06	30
L4R2N4-1	80.7	1.87E-06	30
L4R3N2-1	39.8	1.30E-06	30
L4R3N2-2	39.8	1.01E-06	30
L4R3N2-3	39.8	2.69E-06	30
L4R3N2-4	39.4	1.32E-06	30
L4R3N4-1	199.9	3.82E-06	30
L4R3N4-2	80.7	2.43E-06	30
L4R3N4-3	20.7	2.30E-06	30
L4R3N4-4	39.4	1.45E-06	30
L4R4N2-1	199.9	1.96E-06	30
L4R4N2-2	199.9	3.39E-06	30
L4R4N3-1	199.9	4.40E-06	30
L4R4N4-1	80.7	4.10E-06	30
L4R4N4-2	80.7	3.91E-06	27

the outlet boundary pressure was set to 10^5 Pa while the five inlet pressure used to run the simulations were 1.6×10^5 Pa, 1.7×10^5 Pa, 1.8×10^5 Pa, 1.9×10^5 Pa and 2.0×10^5 Pa. All other input data such as initial permeability, porosity, fluid volume source, viscosity and density as mentioned earlier at the beginning of this section were adopted. Five samples (EGF L3R2N4-3, EGF L3R2N4-4, EGF L3R2N4-7, EGF L3R2N4-8 and EGF L4R3N4-6) from Table 4 and all the three samples (EGF L2R3N1-6, 50N and Nano-10) in Table 5 were selected for the analysis.

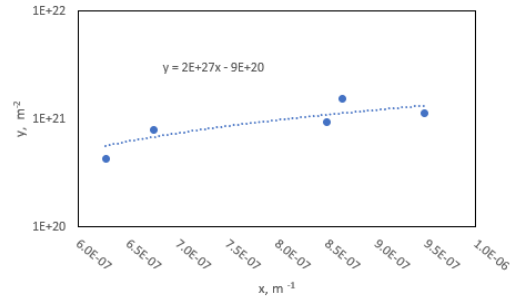


(a)

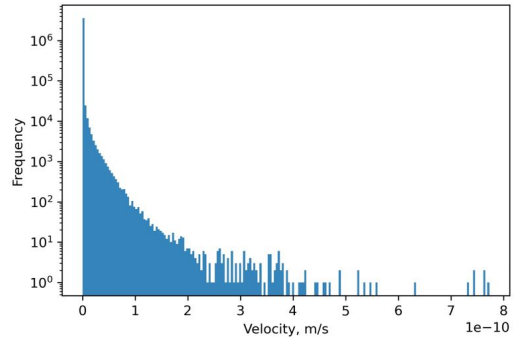


(b)

Figure 23: (a) Determination of permeability and non-Darcy coefficient for sample Nano-10 (b) A typical histogram of velocity magnitude of Nano-10



(a)



(b)

Figure 24: (a) Determination of permeability and non-Darcy coefficient for sample 50N (b) A typical histogram of velocity magnitude of 50N

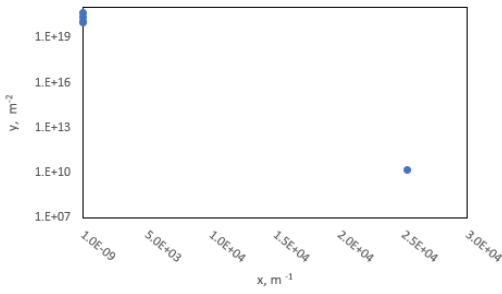
The velocity results obtained from our simulation and input variables listed above were used to generate data for 'y' and 'x' axis in Equation 14. Attempt were made to construct lines of best fit for each sample. From Figures 23 (a) to 30 (a) obtained, this exercise suggests that there is no correlatable relationship between the Non-Darcy equation (Forcheimer) and the simulation data output from this work as the values of permeability and non-Darcy coefficient for some samples are negative. While samples EGF L3R2N4-3, EGF L3R2N4-4, EGF L3R2N4-7, EGF L3R2N4-8 and Nano-10 showed a correlatable values of permeability and non-Darcy coefficient samples EGF L2R3N1-6, EGF L4R3N4-6 and 50N are not in either of the parameter. Both EGF L2R3N1-6 and EGF L4R3N4-6 samples have negative non-Darcy coefficient though the permeability is positive. Whereas 50N sample has positive non-Darcy coefficient but negative permeability.

Also, histogram plotted from each of the simulation run showed that the distribution is an exponential decay (Figures 23 (b) to 30 (b)). Two reasons can be attributed to this (i) the flow regime investigated in this work is within Darcy's limit (ii) porous system is heterogeneous due to shale petrophysical characteristic. To the best of our knowledge, this observation has not been reported in the literature for shale rocks.

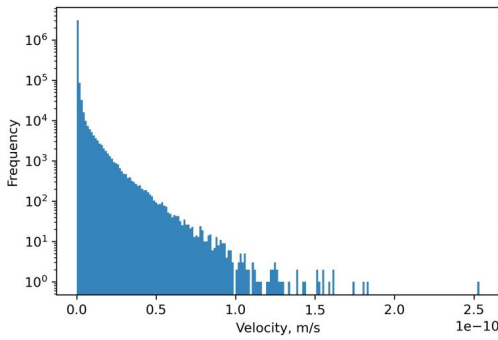
3. Discussions

3.1. Flow heterogeneity characterisation at the pore-scale

Samples highlighted in boxes in Tables 11, 14, and 17 are selected and further sub-cropped (Tables 30 to 37) for simulation purposes. In this section, analysis of pore-scale flow heterogeneity is carried out. The tables give a quick view of the distribution and the variant results of porosity and permeability. Figures 31 to 33 show the pressure and velocity 3D views of NS simulated flow through the selected samples. The velocity and pressure scales are colour-coded as shown by the colour bars. The simulation results (both porosity and permeability) for all the selected samples are presented in Tables 30 to 37. The calculated permeabilities are plotted against porosity for Eagle Ford perpendicular and Eagle Ford parallel nano resolution (Figure 40) and Mancos perpendicular (Figure 41). Figures 40 to 43 are used to investigate whether flow heterogeneity exists in a similar manner to those observed in static model heterogeneity investigation reported in (Adeleye and Akanji, 2017) paper. Sub-sub-samples belonging to the same sub-sample are expected to be clustered in Figures 40 and 41. However, the plots are scattered with outliers which are more pronounced in sub-samples L3R2N4, L4R2N4 and L4R1N3, L4R2N3, L4R2N4, L4R3N2, L4R3N4 for Eagle Ford perpendicular and Mancos perpendicular respectively. Similar observation has been reported in (Adeleye and Akanji, 2017) vis-à-vis voxel method (VOX) and object-oriented bounding box

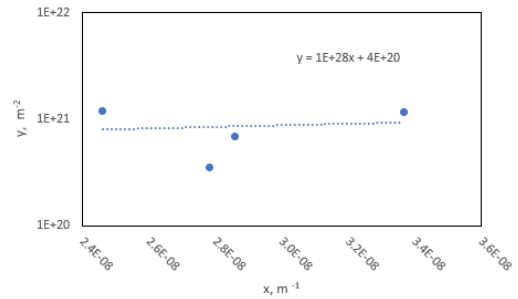


(a)

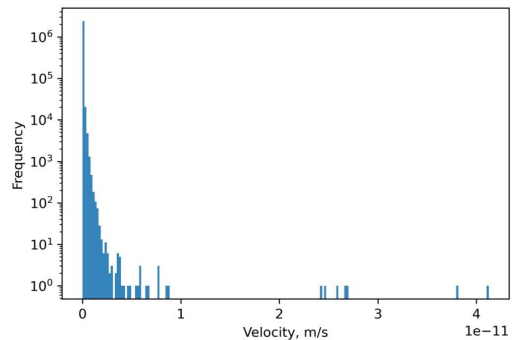


(b)

Figure 25: (a) Determination of permeability and non-Darcy coefficient for sample EGF L2R3N1-6 (b) A typical histogram of velocity magnitude of EGF L2R3N1



(a)



(b)

Figure 26: (a) Determination of permeability and non-Darcy coefficient for sample EGF L3R2N4-3 (b) A typical histogram of velocity magnitude of EGF L3R2N4-3

(OBB) simulation methods. As the simulation was done implicitly on pore network extracted from the images, hence the only contributors here are pores and cracks. The minerals and other entities identified were solely for static identification and their contributions to heterogeneity. However, the impacts of pore heterogeneities on the flow performance were explained mainly through the relationship of tortuosity with porosity and permeability alongside Figures 31 to 33. First, we employed graphical technique and two numerical measures (coefficient of correlation, r and coefficient of determination, R^2) to describe the relationship and effect of porosity and permeability individually on tortuosity.

Tortuosity in porous medium is defined as the geometric property that reflects the actual length of the flow-path at the pore level as the fluid flows around the grain obstacles divided by the length of the porous medium. As simple as this sound, it is however difficult to obtain for complex geometries such as shale. The tortuosity is computed from Carman-Kozeny Equation integrated with Darcy's law as

$$\tau = \left(\frac{L_t}{L} \right)^2 = \frac{\phi r^2}{8K} \quad (15)$$

where r = the average pore radius (m); L_t = tortuous length of the pore network (m); L = the length of the sample (m) Tiab and Donaldson (2004). The computed tortuosity for all Eagle Ford and Mancos sub-sub samples were plotted in scatter diagram with porosity and permeability (Figures 34 to 37).

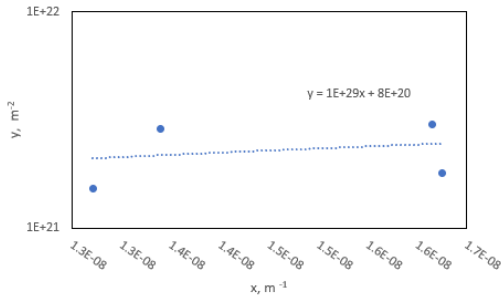
Table 7

Analysis of numerical measure of linear relationship.

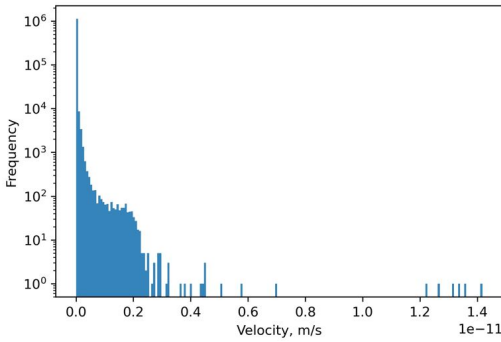
	Tortuosity vs Porosity		Tortuosity vs Permeability	
	Eagle Ford	Mancos	Eagle Ford	Mancos
r	-0.47	-0.13	-0.45	-0.22
R^2	0.22	0.02	0.20	0.05

Figures 34 and 35 show that correlation between tortuosity and porosity is a weak negative linear relationship. This can be substantiated with the r values (Table 7) that have minus signs and the values closer to 0 than to 1. This shows that the flow path of the fluid from one end of the porous medium to the other will be long as the porosity is low and consequently, larger tortuosity. Linear relationship is expected, though it is weak as shale rock is characterized by fine shape changes pores, fine grains, pore bridging and cracks that tend to increase tortuosity. However, the negative relationship can be attributed to isolated pores (non conducting channels) that did not contribute to the flow and to tortuosity indirectly. The R^2 (Table 7) further indicated that the strength of the relationship between porosity and tortuosity is very weak as it revealed that 21.9% and 1.8% of the variations in tortuosity are explained by the pores for Eagle Ford and Mancos respectively. The remaining 78.1% and 98.2% can not be accounted for.

Similarly, tortuosity also has a weak negative linear relationship with permeability (Figures 36 and 37). This is shown by r negative sign and their values (-0.45 and -0.22 for Eagle Ford and Mancos respectively) closer to 0 than to 1. By comparing with Carman-Kozeny Equation, it is ex-

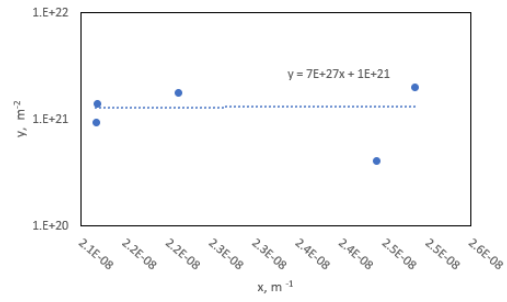


(a)

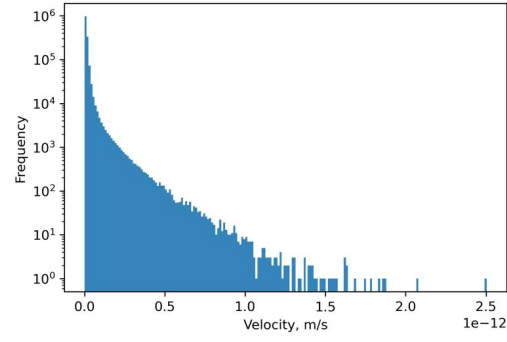


(b)

Figure 27: (a) Determination of permeability and non-Darcy coefficient for sample EGF L3R2N4-4 (b) A typical histogram of velocity magnitude of EGF L3R2N4-4



(a)



(b)

Figure 28: (a) Determination of permeability and non-Darcy coefficient for sample EGF L3R2N4-7 (b) A typical histogram of velocity magnitude of EGF L3R2N4-7

pected that the relationship will be negative but not a weak one. The tortuosity is unstable as it increases with decreasing permeability. It was observed that the relationship of tortuosity with permeability is smoother than with porosity. Unlike porosity, this explained why permeability has direct influence on tortuosity. Statistically, 20.4% and 5% of the variations in tortuosity are accounted for by the permeability while the remaining 79.6% and 95% are unexplained for Eagle Ford and Mancos respectively. With these diagnostic statistical results, it can be inferred that heterogeneity in shale is very high and its permeability greatly influenced tortuosity of the shale rocks. Generally, pores and cracks vary in sizes and so this translates to region of high velocity rate (red colour indicator) to where the fluid is almost stagnant (blue colour indicator, see Figures 31 to 33).

Following the convention established by Carman-Kozeny (Equation 15), we then used computed porosity and permeability from this work to develop regression models for shale. Based on the numerical measure analysed earlier, we used four different combinations (column three in Table 8) of independent variables (porosity and permeability) to get required statistics to pick the best models and assess their fits. Table 8 presents the average of computed tortuosity, the standard error of estimate (S_e), the coefficient of determination (R^2), the F-test of the analysis of variance (F) and the assessment of model in column four to eight respectively. Interested readers are referred to a good statistics textbooks for all equations used in this analysis (Keller, 2014). We assessed all the statistics parameters and inferred that model

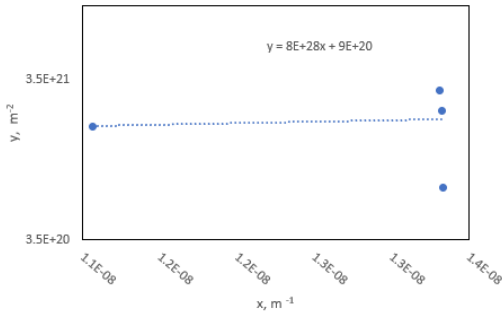
Table 8

Analysis of variance for model assessment.

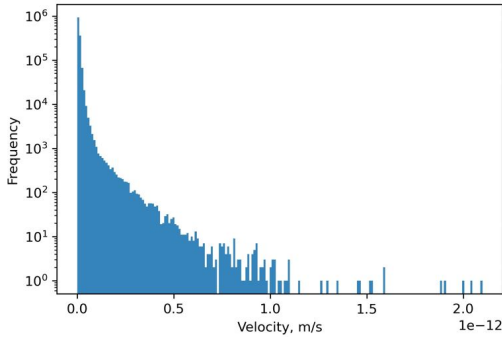
Sample	Model No	Variable combination	Computed τ (mean)	S_e	R^2	F	Assessment of model
EGF PERP	1	$\tau = \phi K$	2.08E+10	4.02E+10	0.374	3.29	Poor
	2	$\tau = \phi/K$	2.08E+10	9.53E+09	0.965	150.81	Very good
	3	$\tau = 1/\phi K$	2.08E+10	9.55E+09	0.965	150.19	Very good
	4	$\tau = r^2/\phi K$	2.08E+10	9.81E+09	0.966	94.97	Good
MAN PERP	1	$\tau = \phi K$	3.22E+10	5.32E+10	0.069	0.894	Poor
	2	$\tau = \phi/K$	3.22E+10	1.89E+10	0.882	90.08	Very good
	3	$\tau = 1/\phi K$	3.22E+10	1.77E+10	0.897	104.9	Very good
	4	$\tau = r^2/\phi K$	3.22E+10	1.53E+10	0.926	96.04	Very good

number three (Table 8) is a good fit for both Eagle Ford and Mancos samples. Hence we presented the models as Equations 16 and 17. Figures 38 and 39 show the comparison of predicted tortuosity from our models versus computed tortuosity obtained from Carman-Kozeny equation for Eagle Ford perpendicular and Mancos perpendicular samples respectively. In Eagle Ford sample (Figure 38), close fittings were experienced in the first eight samples before the gap widens a little bit. In the case of Mancos sample (Figure 39), there were close fittings all through except for sample number 5, 13, 17, 18 21, 22, and 26.

$$\tau = 5980283059.7 + \frac{2.64E - 10}{K} - \frac{100522868900.7}{\phi} \quad (16)$$

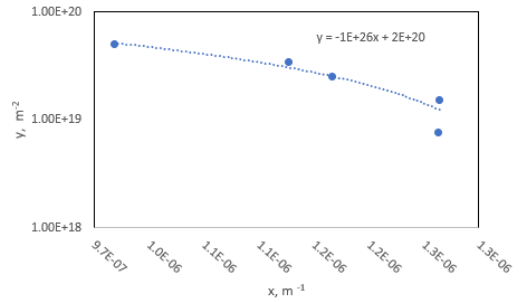


(a)

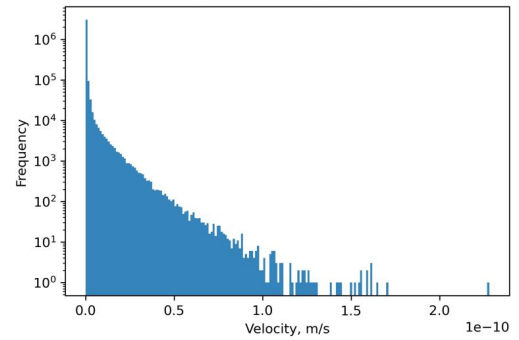


(b)

Figure 29: (a) Determination of permeability and non-Darcy coefficient for sample EGF L3R2N4-8 (b) A typical histogram of velocity magnitude of EGF L3R2N4-8



(a)



(b)

Figure 30: (a) Determination of permeability and non-Darcy coefficient for sample EGF L4R3N4-6 (b) A typical histogram of velocity magnitude of EGF L4R3N4-6

blue, black and green unfilled shapes, while the corresponding filled shapes denote maximum permeability.

$$\tau = 23151493781.7 + \frac{6.79E - 10}{K} - \frac{521678451512.8}{\phi} \quad (17)$$

3.2. Comparison with published work

In order to compare permeability results obtained with available data, the permeabilities calculated across the sub-sub-samples are plotted against the original porosity of the sub-sample. Figure 42 shows permeability against porosity from Eagle Ford perpendicular and Mancos perpendicular (both this work), Gas Research Institute (GRI) crushed rock experimental results, well data results from Eagle Ford as reported by Driskill et al. (2013) and permeability results obtained from LBM (Driskill et al., 2013). Results of permeability obtained in this work are in good agreement with Gas Research Institute (GRI) crushed rock experimental results, well data results from Eagle Ford as reported by Driskill et al. (2013) and permeability results obtained from LBM (Driskill et al., 2013). Specifically, L4R1N2 and L4R4N4 samples from Mancos are within the trend of permeability obtained from both wells (Driskill et al., 2013) considered while sub-samples L3R1N4, L4R2N3 and L4R4N2 are closer compared to the other sub-samples. From Figure 42, it could be seen that the permeabilities of the samples are within the same region as they all clustered together. The minimum permeability of Eagle Ford perpendicular, Mancos perpendicular and Eagle Ford parallel is represented by

The only difference between Eagle Ford and Mancos is their porosities. Though, Eagle Ford parallel nano resolution is exceptional as it has the lowest and highest permeability than other sub-samples. Considering the lowest permeability for each sub-sample, it observed that there is variation in permeability both across the layers and rows as it was also observed in static characterisation. The highest difference within a layer is recorded to be of magnitude 5 for Eagle Ford perpendicular while a magnitude of 2 is recorded for Mancos perpendicular. The same magnitudes were recorded across layers 3 to 4 for Eagle Ford and Mancos perpendicular. The magnitude obtained for Mancos perpendicular has further clarified that outlier did not have significant effects on clustered plots compared to Eagle Ford perpendicular. The approach above is used to make other plots, however, the permeabilities calculated across the sub-sub-samples were normalised with the squared mean grain diameter of the original sub-sample. The minimum and maximum of normalised permeability results were then plotted against the original porosity of the sub-samples alongside the most famous permeability-porosity semi-empirical Kozeny-Carman correlation (Carman, 1956) and other available data (see Figure 43). All samples except for Eagle Ford parallel nano resolution sample estimated permeabilities are lower than Kozeny-Carman correlation. This show a reasonable estimation as our samples are consolidated and expected to have low permeability.

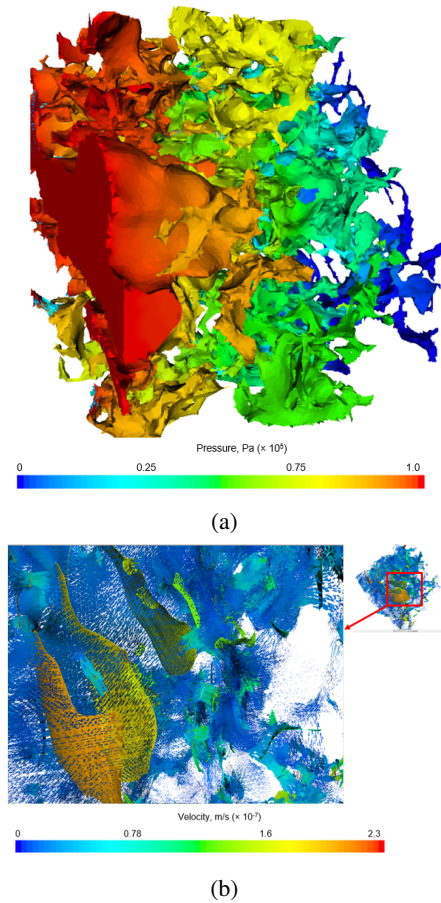


Figure 31: Pressure field and pore velocity distribution computed on the Nano-10 whose finite element is shown in Figure 20 (a) Pressure field, (b) Velocity field distribution. Inset: Enlarged velocity field to show vector arrows.

From Figure 43, a non-dimensional permeability range of $k/D^2 = 1.69 \times 10^{-14}$ to 13.8×10^{-4} for Eagle Ford perpendicular at the porosity range of $\mu = 3.6\% - 28.1\%$ and non-dimensional permeability range of $k/D^2 = 2.25 \times 10^{-11}$ to 5.51×10^{-8} for Mancos perpendicular at the porosity range of $\mu = 3.1\% - 9.8\%$ are obtained. The ranges of permeabilities computed compared very well with ranges of published data from various authors (Table 9). Permeabilities computed for Eagle Ford are within the range though for Mancos our upper boundary is about 23% higher than highest value which was reported by Zhang and Sheng (2017b). This work is thus establishing for the first time that there is an apparent degree of heterogeneity existing in shale rock at the pore scale.

3.3. Evaluation of computational efficiency

Our solution approach was compared with SIMPLE solution approach employed by Liang and Zhang (2016) in terms of the number of iteration steps (IT), CPU times (including the time for assembling the matrices and computing pressure). As most of our model iteration is around 30, we used sub-subsample Mancos perpendicular L3R1N4-1 as the reference. L3R1N4-1 has 3,515,965 elements and its

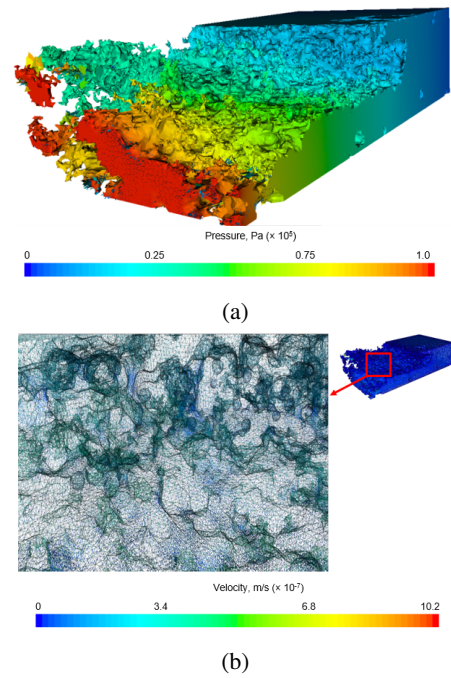


Figure 32: Pressure field and pore velocity field distribution computed on Eagle Ford perpendicular sub-sample L3R2N4-4. (a) Pressure field, (b) Velocity field distribution. Inset: Enlarged velocity field to show vector arrows.

NSE velocity field was calculated within 47.8 seconds at 30 IT, whereas for Liang and Zhang (2016) solution approach it took 82.7 seconds for 16,384 number of elements to converge at IT of 307. Judging by the number of elements, it means their model will require 4.9 hours to run our sample (L3R1N4-1).

The technique adopted in this work is further compared with STAR-CCM+ and ANSYS Fluent. Table 10 show that the proposed Navier-Stokes based technique can handle larger grid numbers in lesser computational time compared with STAR-CCM+ and ANSYS Fluent. This efficiency can be attributed to numerical algorithm technique adopted in this research work. Despite being more computationally efficient and accurate, this technique can be improved to reduce the storage and CPU requirements for constructing 3D tetrahedral elements. Consequently, simulation in much bigger samples would be effectively conducted.

4. Conclusions

In this work, we investigated shale entities, pore morphology and its effect on fluid flow through direct flow simulation within the 3D micro-CT images of Eagle Ford and Mancos. A computational efficient numerical tool was developed based on finite element simulation algorithms to observe the flow characterisation. This new workflow allowed us for the first time to see heterogeneity of shale at the pore scale and computed a larger grid number much more faster when compared with results from various authors. This study

Table 9
Further comparison with other published permeability.

Sample	Permeability (nD)	Method	Scale	Reference
Eagle Ford	1.5 - 885.9	Simulation	Pore	This work
	1 - 37	Lab experiment	Core	Bhandari et al. (2018)
	up to 130000	Well testing	Field	Pap (2014)
	20 - 1200	Well testing	Field	Donaldson et al. (2013)
	66.6 - 320	Lab experiment	Core	Zhang et al. (2017)
Mancos	3.58 - 8621.7	Simulation	Pore	This work
	0.5 - 0.59	Lab experiment	Core	Zhang and Sheng (2017a)
	0.45 - 60	Lab experiment	Core	Zhang et al. (2017)
	0.18 - 0.247	Lab experiment	Core	Lujun et al. (2012)
	0.45 - 7000	Lab experiment	Core	Zhang and Sheng (2017b)

Table 10
Simulation results and computational meshes for Eagle Ford nano resolution.

Reference	Zou et al. (2018)	Shao et al. (2008)	This work
Software	STAR-CCM+	ANSYS Fluent	ANSYS Fluent CSMP CSMP
Grid number	254,800	254,800	20,000 291625* 291625*
Computational time	88.7 (min)	65.6 (min)	5 (days) 10.89 (sec) 10.89 (sec)
Computational power	Six cores and 24 GB memory	Six cores and 24 GB memory	IBM RS/6000 workstation with Power 3 II processor Intel(R) Core(TM) i7-7500U CPU @ 2.70GHz 2.90GHz 16.0 GB memory Intel(R) Xeon(R) CPU E5-2620 v4 @ 2.10GHz II processors 512 GB memory

*Eagle Ford Perpendicular sub-subsample L3N2R4-7 (Figure 33 and Table 4)

establishes the apparent degree of porosity and permeability heterogeneity in shale rock at pore-scale.

- The pore volume distribution shows heterogeneity with consequent effect on permeability of shale rock.
- There is variation in permeability both across the layers and rows just as it was observed in static characterisation.
- The highest difference within a layer is recorded to be of 5 magnitudes for Eagle Ford perpendicular while the magnitude of 2 was recorded for Mancos perpendicular, however, the magnitude of 4 and 1 were recorded across layers for Eagle Ford perpendicular and Mancos perpendicular respectively.
- Tortuosity of shale were obtained from Carman-Kozeny Equation integrated with Darcy's law. It was observed through correlation analysis that porosity and permeability are inversely related to Tortuosity and is also influenced by their heterogeneity nature. Regression models were developed to determine relationship among tortuosity, permeability and porosity for shales and the ones with best assessment values were selected.
- There is no correlatable relationship between the Non-Darcy equation (Forcheimer) and the simulation output data obtained in this work as the values of the permeability and non-Darcy coefficient for some of the samples within a single layer unit are negative. This confirms that the flow is within Darcy's limit and computation of permeability using the Darcy's equation is appropriate.
- The solution of the full Navier-Stokes equation incorporating the convective term allows us to capture the

complexity associated with the heterogeneous nature of the shale formation. This means that though the flow may be steady (time-independent), the motion of the fluid decelerates as it moves down the diverging section of the pore throats (assuming flow is incompressible), thereby indicating acceleration happening over position.

5. Acknowledgement

The authors wish to acknowledge and appreciate the support received from Petroleum Technology Development Fund (PTDF), Nigeria on this project.

A. Porosity estimated after thresholding process

A.1. Volume fraction of organic matter

A.2. Volume fraction of mineral

B. Numerical computation of porosity and permeability from selected samples (samples in boxes from Tables 11, 14, and 17).

B.1. Porosity results

B.2. Permeability results

References

- , 2014. Exploitation of light tight oil plays. *Nafta* 65, 231–237.
- Adeleye, J.O., Akanji, L.T., 2017. Pore-scale analyses of heterogeneity and representative elementary volume for unconventional shale rocks using statistical tools. *Journal of Petroleum Exploration and Production Technology* URL: <https://doi.org/10.1007/s13202-017-0377-4>, doi:10.1007/s13202-017-0377-4.

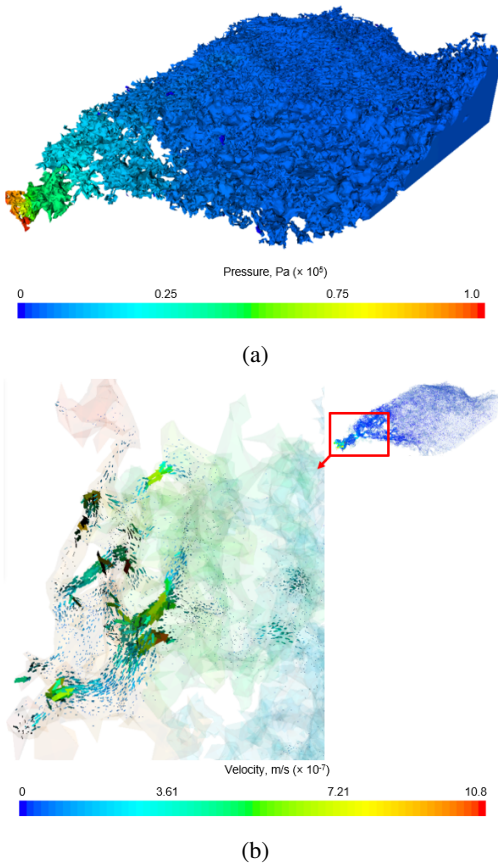


Figure 33: Pressure field and pore velocity field distribution computed on Eagle Ford perpendicular sub-sample L3R2N4-7. (a) Pressure field, (b) Velocity field distribution. Inset: Enlarged velocity field to show vector arrows.

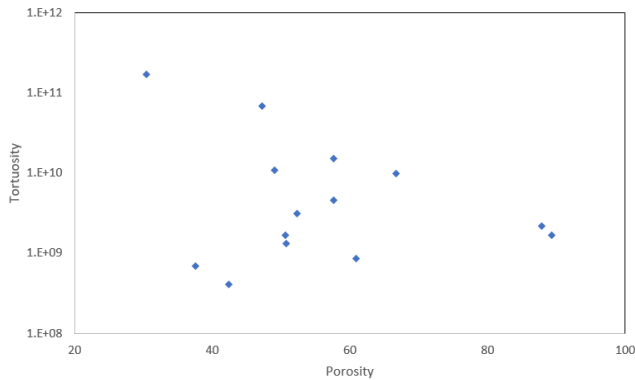


Figure 34: Tortuosity versus porosity correlation for Eagle Ford perpendicular.

Ahmadi, M.M., Mohammadi, S., Hayati, A.N., 2011. Analytical derivation of tortuosity and permeability of monosized spheres: A volume averaging approach. *Physical Review E* 83, 026312. URL: <https://link.aps.org/doi/10.1103/PhysRevE.83.026312>, doi:10.1103/PhysRevE.83.026312.

Akanji, L., Nasr, G., Matthai, S., 2013. Estimation of hydraulic anisotropy of unconsolidated granular packs using finite element methods. *The International Journal of Multiphysics* 7. URL: <http://journal.multiphysics.org/index.php/IJM/article/view/231>, doi:10.1260/1750-9548.7.2.153.

Akanji, L.T., Chidamoio, J., 2020. A finite-element algorithm for Stokes

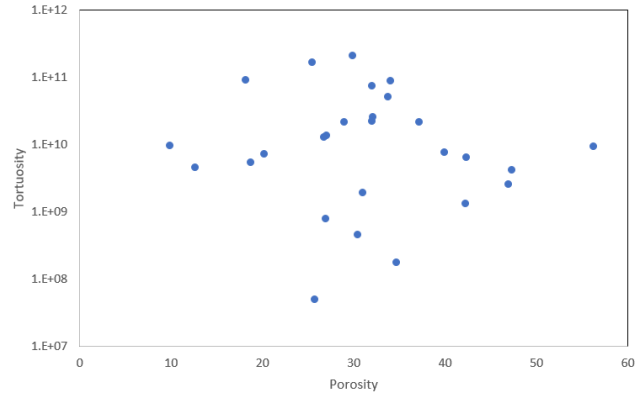


Figure 35: Tortuosity versus porosity correlation for Mancos perpendicular.

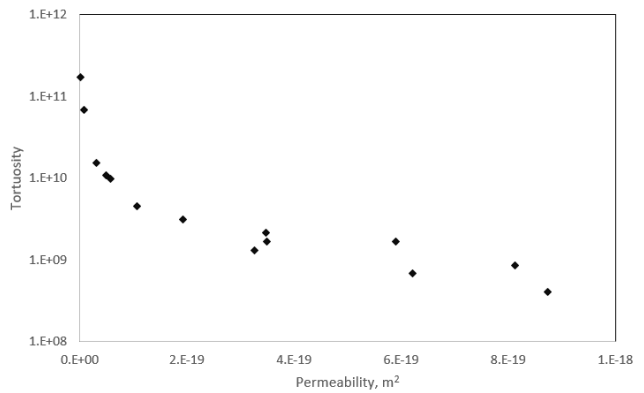


Figure 36: Tortuosity versus permeability correlation for Eagle Ford perpendicular.

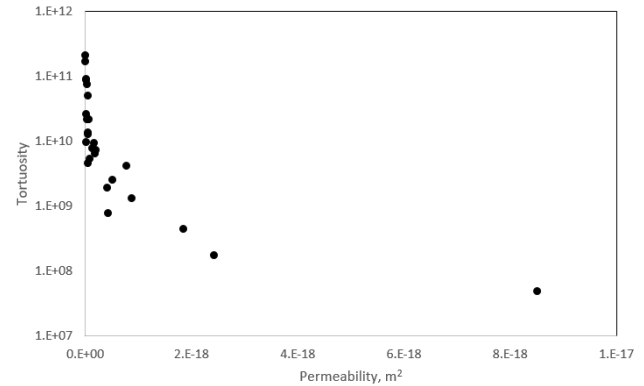


Figure 37: Tortuosity versus permeability correlation for Mancos perpendicular.

flow through oil and gas production tubing of uniform diameter. *Oil Gas Sci. Technol. - Rev. IFP Energies nouvelles* 75, 79. URL: <https://doi.org/10.2516/ogst/2020067>, doi:10.2516/ogst/2020067.

Akanji, L.T., Matthai, S.K., 2009. Finite element-based characterisation of pore-scale geometry and its impact on fluid flow. *Transport Porous Media* 81, 241–259. doi:10.1007/s11242-009-9400-7.

Ali Beskok, G.E.K., 1999. Report: A model for flows in channels, pipes, and ducts at micro and nano scales. *Microscale Thermophysical Engineering* 3, 43–77. URL: <https://doi.org/10.1080/108939599199864>, doi:10.1080/108939599199864,

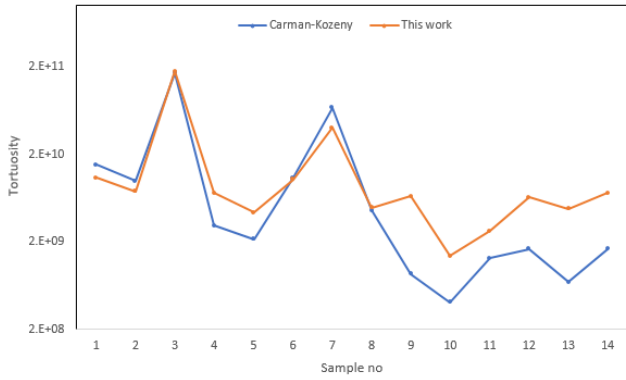


Figure 38: Comparison of predicted versus computed tortuosity for Eagle Ford perpendicular.

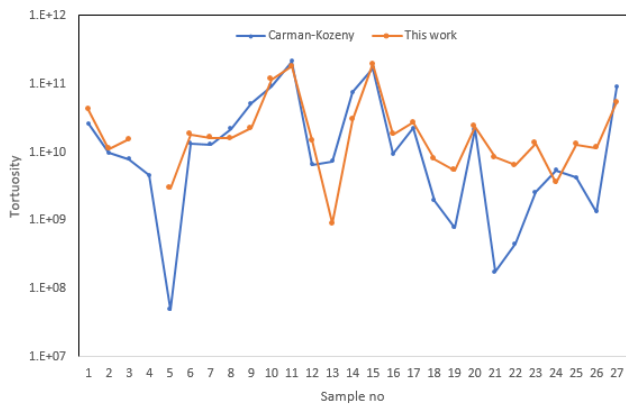


Figure 39: Comparison of predicted versus computed tortuosity for Mancos perpendicular.

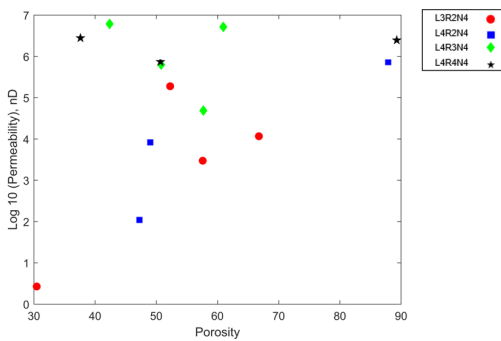


Figure 40: Plot of permeability against total porosity for all Eagle Ford perpendicular shown in Table 4.

arXiv:https://doi.org/10.1080/108939599199864.

Alqahtani, A., Tutuncu, A., 2014. Quantification of total organic carbon content in shale source rocks: An eagle ford case study, Society of Petroleum Engineer. Unconventional Resources Technology Conference. doi:10.15530/URTEC-2014-1921783.

Anderson Jr, J.D., Degroote, J., Degrez, G., Dick, E., Grundmann, R., Vierendeels, J., 2009. Computational Fluid Dynamics: An introduction. 3rd ed., Springer.

Bear, J., 1972. Dynamics of Fluids In Porous Media. Number v. 1 in Dynamics of Fluids in Porous Media, American Elsevier Publishing Company. URL: https://books.google.co.uk/books?id=9JVRAAAAMAAJ.

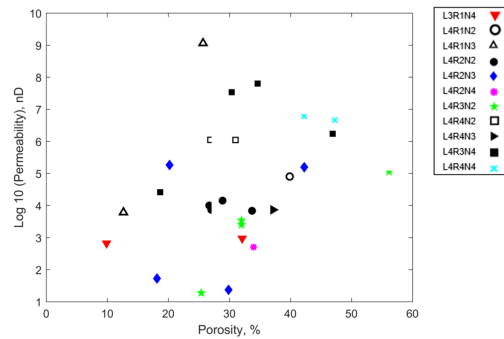


Figure 41: Plot of permeability against total porosity for all the Mancos perpendicular shown in Table 6.

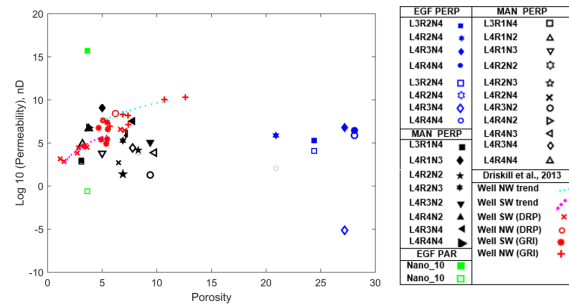


Figure 42: Plot of permeability against total porosity from this work (Eagle Ford perpendicular, Mancos perpendicular, Eagle Ford parallel sub-samples), results from Gas Research Institute (GRI) crushed rock experimental analysis and well data from Eagle Ford as reported by Driskill et al. (2013) and permeability results obtained from LBM (Driskill et al., 2013). Where, the minimum permeability of Eagle Ford perpendicular, Mancos perpendicular and Eagle Ford parallel are represented by blue, black and green unfilled shapes respectively, while the corresponding filled shapes denote maximum permeability.

Belvalkar, R.A., Oyewole, S., 2010. Development of marcellus shale in pennsylvania, Society of Petroleum Engineers. Society of Petroleum Engineers. doi:10.2118/134852-MS.

Bhandari, A.R., Flemings, P.B., Hofmann, R., Polito, P.J., 2018. Stress-dependent in situ gas permeability in the eagle ford shale. Transport in Porous Media .

Bhandari, A.R., Flemings, P.B., Polito, P.J., Cronin, M.B., Bryant, S.L., 2015. Anisotropy and stress dependence of permeability in the barnett shale. Transport in Porous Media 108, 393–411. doi:10.1007/s11242-015-0482-0.

Blunt, M.J., Bijeljic, B., Dong, H., Gharbi, O., Iglauer, S., Mostaghimi, P., Paluszny, A., Pentland, C., 2013. Pore-scale imaging and modelling. Advances in Water Resources 51, 197 – 216. URL: http://www.sciencedirect.com/science/article/pii/S0309170812000528, doi:https://doi.org/10.1016/j.advwatres.2012.03.003. 35th Year Anniversary Issue.

Bruner, K.R., Smosna, R., 2011. A comparative study of the Mississippian Barnett shale, Fort Worth Basin, and Devonian Marcellus Shale, Appalachian Basin. Technical Report. U.S. Department of Energy. doi:DOE/NETL-2011/1478.

Brush, D.J., Thomson, N.R., 2003. Fluid flow in synthetic rough-walled fractures: Navier-stokes, stokes, and local cubic law simulations. Water Resour. Res 39, 1085. doi:10.1029/2002WR001346.

Bryant, S., Blunt, M., 1992. Prediction of relative permeability in simple porous media. Phys. Rev. A 46, 2004–2011. URL: https://link.aps.org/doi/10.1103/PhysRevA.46.2004, doi:10.1103/PhysRevA.46.2004.

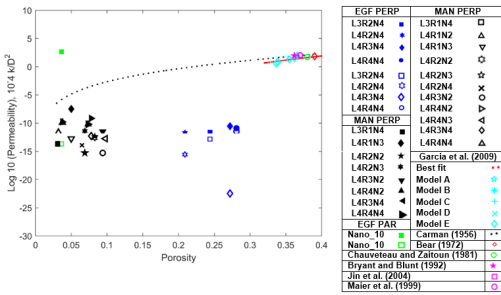


Figure 43: Plot of normalised permeability against total porosity for Eagle Ford perpendicular, Mancos perpendicular and Eagle Ford parallel sub-samples, synthetic model samples A, B, C, D and E and the best fit data of their work (Garcia et al., 2009), beads and unconsolidated sands (Chauveteau and Zaitoun, 1981), monosized sphere packs (Bryant and Blunt, 1992; Maier et al., 1999), unconsolidated and consolidated reservoir rock (Jin et al., 2004), empirical Kozeny-Carman correlation (Carman, 1956) and sands of different heterogeneity (Bear, 1972).

Table 11
Estimates of porosity for the three-dimensional volume of 96 subsamples of Eagle Ford perpendicular.

	Layer 1	Layer 2	Layer 3	Layer 4	Layer 5	Layer 6
R1N1	0.002	2.1E-03	1.2E-02	3.1E-02	7.0E-02	5.8E-02
R1N2	0.04	3.3E-02	0.11	0.29	0.58	0.53
R1N3	0.07	6.4E-02	0.38	0.86	1.04	1.0
R1N4	0.03	2.7E-02	16.0	12.0	0.51	0.4
R2N1	0.02	1.8E-02	6.0E-02	0.2	0.4	0.31
R2N2	0.15	0.38	0.36	0.94	1.86	2.3
R2N3	0.24	0.13	0.89	2.55	2.81	3.6
R2N4	0.15	0.18	24.4	20.9	1.9	1.9
R3N1	3.1E-02	3.3E-02	0.11	0.22	0.36	0.36
R3N2	0.21	0.23	0.48	1.1	1.9	2.76
R3N3	0.24	0.37	0.65	5.5	3.2	4.1
R3N4	0.18	0.21	12.1	27.2	2.01	2.1
R4N1	3.6E-03	5.6E-03	2.3E-02	2.9E-02	7.7E-02	8.4E-02
R4N2	6.8E-02	6.5E-02	0.2	0.4	0.74	0.77
R4N3	0.11	0.1	0.32	12.48	1.3	1.48
R4N4	3.8E-02	5.5E-02	4.4	28.1	0.7	0.7

Average porosity = 2.28 %

Table 12
Estimates of porosity by segmenting the three-dimensional volume of Layer 3 subsamples of Eagle Ford perpendicular 1.

	N1	N2	N3	N4
R1	0.01	0.11	0.38	16.0
R2	0.06	0.36	0.89	1.45
				1.9
				48.2
				62.8
R3	0.11	0.48	0.65	12.1
				0.85
				1.7
R4	0.023	0.19	0.32	4.45

Carman, P., 1956. Flow of Gases Fluids in Porous Media. Academic Press, New York.,
 Chauveteau, G., Zaitoun, A., 1981. Basic rheological behavior of xanthan polysaccharide solutions in porous media: Effects of pore size and polymer concentration.
 Chen, J., Wei, D., Yang, W., 2013. Integration of different imaging methodologies to study shale sample heterogeneity, Unconventional Resources Technology Conference. Society of Petroleum Engineering.
 Civan, F., Rai, C.S., Sondergeld, C.H., 2012. Determining shale perme-

Table 13
Estimates of porosity for the three-dimensional volume of 96 subsamples of Mancos parallel.

	Layer 1	Layer 2	Layer 3	Layer 4	Layer 5	Layer 6
R1N1	1.5E-03	5.3E-04	8.9E-04	2.5E-03	5.5E-03	2.0E-03
R1N2	5.8E-03	8.0E-03	1.2E-02	2.9E-02	4.8E-02	4.2E-02
R1N3	1.5E-02	1.1E-02	2.2E-02	4.0E-02	8.3E-02	1.1E-01
R1N4	8.7E-03	6.7E-03	1.3E-02	4.2E-02	3.0E-02	3.9E-02
R2N1	3.2E-03	3.3E-03	7.0E-03	1.6E-02	1.8E-02	1.9E-02
R2N2	3.5E-02	4.3E-02	6.8E-02	1.0E-01	1.7E-01	1.8E-01
R2N3	5.7E-02	7.2E-02	0.1	2.4E-01	3.0E-01	3.7E-01
R2N4	6.9E-02	4.3E-02	5.9E-02	1.5E-01	2.7E-01	1.7E-01
R3N1	2.1E-02	1.2E-02	1.4E-02	3.1E-02	2.7E-02	3.3E-02
R3N2	1.4E-01	2.3E-02	9.2E-02	1.4E-01	2.1E-01	2.4E-01
R3N3	1.2E-01	1.2E-01	1.6E-01	3.0E-01	6.1E-01	4.9E-01
R3N4	4.4E-02	5.8E-02	7.2E-02	1.2E-01	2.1E-01	2.3E-01
R4N1	3.5E-02	3.5E-02	1.2E-01	4.5E-01	3.9E-02	1.1E-01
R4N2	2.1E-01	2.0E-01	2.3E-01	2.3E-01	1.8E-01	2.2E-01
R4N3	9.4E-02	1.8E-01	1.6E-01	1.7E-01	2.1E-01	1.7E-01
R4N4	2.7E-02	8.1E-02	1.1E-01	9.6E-02	7.3E-02	5.8E-02

Average porosity = 0.106 %

Table 14
Estimates of porosity for the three-dimensional volume of 96 subsamples of Mancos perpendicular.

	Layer 1	Layer 2	Layer 3	Layer 4	Layer 5	Layer 6
R1N1	0.0	0.0	2.1E-01	3.2E-02	0.0	0.0
R1N2	0.0	0.0	9.9E-01	3.2	0.0	0.0
R1N3	0.0	0.0	2.1	5.0	0.0	0.0
R1N4	0.0	0.0	3.1	1.9	0.0	0.0
R2N1	0.0	0.0	7.7E-01	2.0	0.0	0.0
R2N2	0.0	0.0	1.5E-03	8.3	0.0	0.0
R2N3	0.0	0.0	0	6.9	3.0E-05	0.00E+00
R2N4	0.0	0.0	4.6E-01	6.5	0.0	0.0
R3N1	0.0	0.0	4.9E-02	3.3	0.0	0.0
R3N2	0.0	0.0	0.0E+00	9.4	0.0	0.0
R3N3	0.0	0.0	0.0E+00	1.1E+01	0.0	0.0
R3N4	0.0	0.0	0.0E+00	7.79	0.0	0.0
R4N1	0.0	0.0	1.6E-03	1.06	0.0	0.0
R4N2	0.0	0.0	0.0E+00	7.35	0.0	0.0
R4N3	0.0	3.0E-05	0.0	9.78	0.0	0.0
R4N4	0.0	0.0	0.0	3.77	0.0	0.0

Average porosity = 0.99 %

ability to gas by simultaneous analysis of various pressure tests, Society of Petroleum Engineers. Society of Petroleum Engineers. doi:10.2118/144253-PA.
 Clarkon, C., Nobakht, M., Kaviani, D., Ertekin, T., 2012. Production analysis of tight-gas and shale-gas reservoirs using the dynamic-slippage concept. SPE Journal 17, 230–242. doi:10.2118/144317-PA.
 Curtis, M.E., Carl, H.S., Ambrose, R.J., Rai, C.S., 2012. Microstructural investigation of gas shales in two and three dimensions using nanometer-scale resolution imaging, American Association of Petroleum Geologists. American Association of Petroleum Geologists. pp. 665–677. doi:10.1306/08151110188.
 Djebbar, T., Donaldson, E.C., 1996. Petrophysics: Theory and practice of measuring reservoir rock and fluid transport properties.
 Donaldson, E.C., Alam, W., Begum, N., 2013. Chapter 5 - field implementation of hydraulic fracturing, in: Donaldson, E.C., Alam, W., Begum, N. (Eds.), Hydraulic Fracturing Explained. Gulf Publishing Company, pp. 95–116. URL: https://www.sciencedirect.com/science/article/pii/B9781933762401500143, doi:https://doi.org/10.1016/B978-1-933762-40-1.50014-3.
 Driskill, B., Walls, J., DeVito, J., Sinclair, S.W., 2013. Applications of sem imaging to reservoir characterization in the eagle ford shale, south

Table 15

Estimates of porosity for the three-dimensional volume of 96 subsamples of Marcellus parallel.

	Layer 1	Layer 2	Layer 3	Layer 4	Layer 5	Layer 6
R1N1	0.0	0.0	0.0	0.0	0.0	0.0
R1N2	0.0	0.0	0.0	0.0	0.0	0.0
R1N3	0.0	0.0	0.0	0.0	2.96E-05	0.0
R1N4	0.0	0.0	0.0	0.0	0.0	3.0E-05
R2N1	0.0	0.0	0.0	3.0E-05	3.0E-05	0.0
R2N2	0.0	5.9E-05	3.0E-05	8.9E-05	3.0E-05	0.0
R2N3	0.0	0.0	0	0.0	1.2E-04	2.4E-04
R2N4	0.0	0.0	0	0.0	8.9E-05	3.0E-05
R3N1	0.0	0.0	0	8.9E-05	0.0	0.0
R3N2	0.0	0.0	3.0E-05	3.6E-04	0.0	1.5E-04
R3N3	0.0	0.0	3.0E-05	3.6E-04	3.6E-04	3.0E-04
R3N4	0.0	0.0	5.9E-05	5.9E-05	3.0E-05	9.0E-05
R4N1	0.0	0.0	0.0	0.0	0.0	0.0
R4N2	0.0	0.0	0.0	0.0	0.0	0.0
R4N3	0.0	0.0	3.0E-05	3.0E-05	3.0E-05	3.0E-05
R4N4	0.0	0.0	0.0	0.00E+00	3.0E-05	0.0
Average porosity = 2.96E-05 %						

Table 16

Estimates of porosity for the three-dimensional volume of 96 subsamples of Marcellus perpendicular.

	Layer 1	Layer 2	Layer 3	Layer 4	Layer 5	Layer 6
R1N1	3.9E-04	3.0E-05	3.0E-05	2.1E-04	2.1E-04	8.9E-05
R1N2	6.5E-04	7.7E-04	1.5E-03	2.3E-03	3.6E-03	3.6E-03
R1N3	1.3E-03	1.7E-03	2.7E-03	3.8E-03	8.1E-03	9.0E-03
R1N4	3.9E-04	5.0E-04	1.9E-03	2.3E-03	3.1E-03	3.7E-03
R2N1	4.7E-04	3.0E-04	1.2E-03	2.0E-03	4.4E-03	3.1E-03
R2N2	4.6E-03	5.5E-03	8.5E-03	1.2E-02	2.5E-02	3.6E-02
R2N3	5.8E-03	9.7E-03	1.5E-02	2.1E-02	4.9E-02	7.3E-02
R2N4	3.9E-03	3.5E-03	6.8E-03	1.0E-02	2.1E-02	2.9E-02
R3N1	5.9E-04	7.7E-04	1.5E-03	2.0E-03	5.8E-03	4.6E-03
R3N2	5.4E-03	7.9E-03	1.3E-02	1.6E-02	4.3E-02	4.9E-02
R3N3	9.7E-03	3.0E-02	3.8E-02	5.6E-02	9.3E-02	1.2E-01
R3N4	4.6E-03	8.3E-02	1.1E-02	1.5E-02	2.9E-02	4.0E-02
R4N1	1.8E-04	1.5E-04	2.1E-04	3.9E-04	1.5E-03	1.1E-03
R4N2	2.2E-03	2.2E-03	4.5E-03	8.8E-03	1.6E-02	1.3E-02
R4N3	3.9E-03	4.7E-03	7.8E-03	1.1E-02	3.6E-02	2.8E-02
R4N4	1.0E-03	1.7E-03	3.9E-03	6.0E-03	2.2E-02	1.1E-02
Average porosity = 0.013 %						

Table 17

Estimates of porosity for the three-dimensional volume of 12 sub-samples of Eagle Ford parallel at 750 nm resolution.

	R1N1	R1N2	R2N1	R2N2	R3N1	R3N2
Layer 1	1.28	1.43	0.54	1.47	2.45	1.11
Layer 2	1.03	2.07	1.83	1.89	3.86	1.95
Average porosity = 1.74 %						

Table 18

Estimates of volume fraction of organic matter for the three-dimensional volume of 96 subsamples of Eagle Ford parallel

	Layer 1	Layer 2	Layer 3	Layer 4	Layer 5	Layer 6
R1N1	1.8E-02	8.4E-03	2.6E-02	7.1E-02	2.0E-01	3.3E-01
R1N2	4.3E-02	7.4E-02	1.9E-01	4.3E-01	1.0	1.9E+00
R1N3	1.9E-01	2.0E-01	4.3E-01	6.6E-01	1.4	2.5
R1N4	2.8E-02	4.4E-02	7.5E-02	1.6E-01	4.7E-01	9.0E-01
R2N1	5.4E-02	8.4E-02	1.5E-01	3.5E-01	8.9E-01	1.5
R2N2	4.2E-01	3.3E-01	7.4E-01	2.0	3.6	6.1
R2N3	5.4E-01	6.1E-01	1.0E+00	1.8E+00	3.8E+00	6.8
R2N4	6.1E-02	9.1E-02	2.5E-01	6.1E-01	1.5	2.9
R3N1	4.6E-02	6.4E-02	1.7E-01	4.2E-01	9.8E-01	1.8
R3N2	6.4E-01	6.5E-01	1.1	2.2	3.7	5.8
R3N3	3.6E-01	4.8E-01	9.7E-01	2.0	3.8	7.0
R3N4	1.4E-01	2.3E-01	4.5E-01	1.0	2.5	3.9
R4N1	7.5E-02	9.0E-02	1.9E-01	2.8E-01	5.5E-01	8.1E-01
R4N2	1.5E-01	1.8E-01	4.0E-01	7.2E-01	1.5	2.6
R4N3	7.9E-02	1.5E-01	3.1E-01	7.3E-01	1.7	2.9
R4N4	8.2E-02	1.5E-01	2.4E-01	4.2E-01	1.1	1.8E
Average volume fraction = 1.09 %						

Table 19

Estimates of volume fraction of organic matter for the three-dimensional volume of 96 subsamples of Eagle Ford perpendicular 1.

	Layer 1	Layer 2	Layer 3	Layer 4	Layer 5	Layer 6
R1N1	5.2E-02	6.1E-02	2.2E-01	7.6E-01	1.3E+00	1.1E+00
R1N2	6.2E-01	6.3E-01	1.6	4.5	7.6	6.5
R1N3	1.0	1.02	2.9	1.0E+01	1.2E+01	1.1E+01
R1N4	4.9E-01	5.0E-01	7.5	1.1E+01	7.2	5.4
R2N1	3.9E-01	3.8E-01	8.73E-01	3.4	5.3	4.4
R2N2	1.98	2.3	3.8	1.1E+01	1.8E+01	1.9E+01
R2N3	2.79	3.8	6.1	1.8E+01	2.3E+01	2.5E+01
R2N4	2.0	2.5	7.4	20	18.6	16.3
R3N1	5.2E-01	5.9E-01	1.5	3.68	5.4	4.8
R3N2	2.6	2.9	4.8	12.9	17.9	21.3
R3N3	2.8	4.01	5.9	21.6	24.2	25.3
R3N4	2.3	2.78	7.9	18.4	19	17.2
R4N1	9.45E-02	1.4E-01	4.3E-01	7.0E-01	1.6	1.47
R4N2	1.1	1.0	2.2	6.3	9.0	8.6
R4N3	1.5	1.9	3.63	12.4	13.7	13.4
R4N4	6.6E-01	9.0E-01	3.1	11.3	9.0	7.9
Average volume fraction = 6.79 %						

Gupta, N., Mishra, B., 2017. Creep Characterization of Marcellus Shale. Technical Report.

Javadpour, F., 2009. Nanopores and apparent permeability of gas flow in mudrocks (shales and siltstone). Journal of Canadian Petroleum Technology 48, 16–21. doi:10.2118/09-08-16-DA.

Jennings, D.S., Antia, J., 2013. Petrographic characterization of the eagle ford shale, south texas: Mineralogy, common constituents, and distribution of nanometer-scale pore types, in w. camp, e. diaz, and b. wawak, eds., electron microscopy of shale hydrocarbon reservoirs, The American Association of Petroleum Geologists. The American Association of Petroleum Geologists. pp. 101–113. doi:10.1306/13391708M1023586.

Jin, G., Patzek, T.W., Silin, D.B., 2004. Direct prediction of the absolute permeability of unconsolidated and consolidated reservoir rock, Society of Petroleum Engineers. in Proceedings SPE Annual Technical Conference and Exhibition. doi:doi:10.2118/90084-MS.

Kazemi, M., Ali, T.B., 2015. Predicting gas apparent permeability of shale samples: A novel analytical approach doi:10.2118/175035-MS.

Keller, G., 2014. Statistics for Management and Economics. Number v. 2 in Statistics for Management and Economics, Cengage Learning. URL: https://books.google.je/books?id=Rw-FCwAAQBAJ.

Liang, Z.Z., Zhang, G.F., 2016. Simple-like preconditioners for saddle point problems from the steady navier–stokes equations. Journal of Computational and Applied Mathematics 302, 211 – 223. URL:

texas, usa. The american association of petroleum geologists doi:10.1306/13391709M1023587.

Eker, I., Kurtoglu, B., Kazemi, H., 2014. Multiphase rate transient analysis in unconventional reservoirs: Theory and applications, Society of Petroleum Engineers. Society of Petroleum Engineers. doi:10.2118/171657-MS.

Florence, F.A., Rushing, J., Newsham, K.E., Blasingame, T.A., et al., 2007. Improved permeability prediction relations for low permeability sands, in: Rocky mountain oil & gas technology symposium, Society of Petroleum Engineers.

Garcia, X., Akanji, L.T., Blunt, M.J., Matthai, S.K., Latham, J.P., 2009. Numerical study of the effects of particle shape and polydispersity on permeability. Phys. Rev. E 80, 021304. URL: https://link.aps.org/doi/10.1103/PhysRevE.80.021304, doi:10.1103/PhysRevE.80.021304.

Table 20

Estimates of volume fraction of organic matter for the three-dimensional volume of 96 subsamples of Mancos parallel 2.

	Layer 1	Layer 2	Layer 3	Layer 4	Layer 5	Layer 6
R1N1	3.7E-02	4.6E-02	1.0E-01	1.8E-01	2.5E-01	1.8E-01
R1N2	2.9E-01	4.1E-01	7.3E-01	1.3	1.96	1.83
R1N3	5.6E-01	6.9E-01	1.1	1.78	2.80	3.04
R1N4	3.5E-01	3.8E-01	6.0E-01	1.0	1.3	1.33
R2N1	2.5E-01	3.5E-01	5.7E-01	9.5E-01	1.16	1.12
R2N2	1.6	2.1	2.95	4.09	5.82	5.91
R2N3	2.1	3.1	4.0	6.1	8.8	9.9
R2N4	1.6	1.7	2.51	3.87	5.61	5.53
R3N1	5.5E-01	5.9E-01	8.66E-01	1.36	1.62	1.57
R3N2	2.7	1.8	3.73	5.25	6.91	7.48
R3N3	3.1	4.3	5.28	7.90	11.2	12.0
R3N4	2.0	2.6	3.07	4.61	6.72	7.18
R4N1	4.0E-01	3.6E-01	4.75E-01	1.33	7.9E-01	9.5E-01
R4N2	1.3	1.7	2.2	3.1	3.7	3.6
R4N3	1.8	2.3	3.24	4.26	4.96	5.13
R4N4	9.1E-01	1.3	2.1	2.5	2.8	2.7

Average volume fraction = 2.73 %

Table 22

Estimates of volume fraction of organic matter for the three-dimensional volume of 96 subsamples of Marcellus parallel 2.

	Layer 1	Layer 2	Layer 3	Layer 4	Layer 5	Layer 6
R1N1	1.2E-03	1.3E-03	3.6E-03	9.1E-03	1.1E-02	8.8E-03
R1N2	1.0E-02	1.6E-02	3.9E-02	6.9E-02	1.1E-01	1.0E-01
R1N3	2.1E-02	3.7E-02	8.4E-02	1.3E-01	2.1E-01	2.3E-01
R1N4	1.0E-02	1.9E-02	3.9E-02	7.5E-02	1.3E-01	1.3E-01
R2N1	6.2E-03	9.0E-03	2.5E-02	2.2E-01	6.9E-02	6.5E-02
R2N2	4.4E-02	7.6E-02	1.3E-01	3.8E-01	3.9E-01	5.0E-01
R2N3	6.5E-02	1.4E-01	2.5E-01	2.7E-01	6.3E-01	9.2E-01
R2N4	5.1E-02	8.4E-02	1.6E-01	5.0E-02	4.6E-01	5.9E-01
R3N1	7.5E-03	1.1E-02	2.5E-02	2.6E-01	8.0E-02	7.8E-02
R3N2	4.9E-02	8.3E-02	1.5E-01	4.5E-01	4.3E-01	5.5E-01
R3N3	7.5E-02	1.5E-01	2.7E-01	4.5E-01	7.6E-01	1.0E+00
R3N4	5.3E-02	9.0E-02	1.6E-01	3.0E-01	4.8E-01	5.6E-01
R4N1	1.5E-03	1.6E-03	6.0E-03	1.1E-02	2.0E-02	1.6E-02
R4N2	1.4E-02	2.4E-02	5.3E-02	1.0E-01	1.6E-01	1.6E-01
R4N3	3.4E-02	4.4E-02	9.3E-02	1.6E-01	2.7E-01	3.0E-01
R4N4	1.3E-02	2.3E-02	6.2E-02	1.1E-01	1.5E-01	1.5E-01

Average volume fraction = 0.162 %

Table 21

Estimates of volume fraction of organic matter for the three-dimensional volume of 96 subsamples of Mancos perpendicular 1.

	Layer 1	Layer 2	Layer 3	Layer 4	Layer 5	Layer 6
R1N1	0.0	2.1E-04	2.0	7.6E-02	2.7E-03	3.0E-05
R1N2	5.5E-03	5.6E-04	3.3	3.8	3.8E-03	1.2E-04
R1N3	5.9E-05	6.1E-03	2.13	4.3	9.8E-03	3.6E-03
R1N4	3.0E-05	1.0E-03	5.5	2.5	2.8E-03	2.7E-04
R2N1	3.0E-04	7.4E-03	3.9	3.5	5.0E-04	5.9E-05
R2N2	1.1E-03	2.4E-03	2.3E-02	5.7	3.2E-03	2.7E-04
R2N3	6.2E-04	8.8E-03	5.8E-03	6.8	3.2E-02	9.2E-03
R2N4	5.9E-05	1.2E-03	3.0E-01	6.6	4.8E-03	6.5E-04
R3N1	3.0E-04	5.4E-03	8.7E-01	6.4	4.8E-03	8.9E-05
R3N2	6.5E-04	9.0E-03	1.4E-03	5.0	1.9E-03	1.5E-03
R3N3	3.3E-03	8.0E-04	4.2E-03	4.2	5.1E-02	4.9E-03
R3N4	2.6E-03	5.6E-04	3.2E-03	6.6	4.0E-02	2.1E-03
R4N1	1.2E-04	1.9E-03	1.2E-01	4.8	2.1E-03	5.9E-05
R4N2	1.2E-04	4.4E-04	2.0E-03	6.9	9.9E-03	3.1E-03
R4N3	1.1E-03	1.6E-02	6.3E-03	5.2	2.1E-02	2.7E-03
R4N4	2.1E-04	3.8E-03	3.0E-04	9.6	1.2E-03	3.3E-04

Average volume fraction = 1.04 %

Table 23

Estimates of volume fraction of organic matter for the three-dimensional volume of 96 subsamples of Marcellus perpendicular 2.

	Layer 1	Layer 2	Layer 3	Layer 4	Layer 5	Layer 6
R1N1	3.3E-02	1.2E-02	3.4E-02	6.0E-02	9.0E-02	7.7E-02
R1N2	1.2E-01	1.6E-01	2.9E-01	4.0E-01	6.2E-01	6.3E-01
R1N3	1.9E-01	2.7E-01	4.3E-01	5.6E-01	1.0E+00	1.1E+00
R1N4	7.3E-02	1.1E-01	2.6E-01	3.1E-01	5.3E-01	5.9E-01
R2N1	8.2E-02	1.3E-01	2.4E-01	3.0E-01	5.3E-01	5.0E-01
R2N2	5.6E-01	7.2E-01	1.0E+00	1.3E+00	2.5E+00	3.3E+00
R2N3	6.8E-01	1.1E+00	1.5E+00	1.9E+00	3.6E+00	5.3E+00
R2N4	4.5E-01	6.3E-01	9.4E-01	1.2E+00	2.1E+00	2.7E+00
R3N1	1.2E-01	1.6E-01	2.9E-01	3.9E-01	8.1E-01	7.8E-01
R3N2	6.5E-01	1.0E+00	1.4E+00	1.7E+00	3.3E+00	4.3E+00
R3N3	8.6E-01	1.7E+00	2.1E+00	2.8E+00	5.1E+00	7.0E+00
R3N4	5.9E-01	9.0E-01	1.2E+00	1.5E+00	2.8E+00	3.5E+00
R4N1	3.4E-02	5.3E-02	1.1E-01	1.6E-01	3.4E-01	2.6E-01
R4N2	3.2E-01	4.3E-01	7.3E-01	9.3E-01	1.8E+00	1.8E+00
R4N3	5.7E-01	7.2E-01	1.1E+00	1.4E+00	2.6E+00	2.9E+00
R4N4	2.5E-01	3.6E-01	6.0E-01	6.0E-01	1.4E+00	1.4E+00

Average volume fraction = 1.11 %

<http://www.sciencedirect.com/science/article/pii/S0377042716300590>,
doi:<https://doi.org/10.1016/j.cam.2016.02.012>.

Lujun, J., Quan, G., Jim, F., Rui, Z., Martin, C., Mukul, S., 2012. Drilling unconventional shales with innovative water-based mud-part i: Evaluation of nanoparticles as a physical shale inhibitor, American Association of Drilling Engineers.

Ma, L., Taylor, K.G., Lee, P.D., Dobson, K.J., Dowey, P.J., Courtois, L., 2016. Novel 3d centimetre-to nano-scale quantification of an organic-rich mudstone: The carboniferous bowland shale, northern england. Marine and Petroleum Geology 72, 193–205. doi:[10.1016/j.marpetgeo.2016.02.008](https://doi.org/10.1016/j.marpetgeo.2016.02.008).

Maier, R.S., Kroll, D.M., Davis, H., Bernard, R.S., 1999. Simulation of flow in bidisperse sphere packings. Journal of Colloid and Interface Science 217, 341 – 347. URL: <http://www.sciencedirect.com/science/article/pii/S0021979799963725>, doi:<https://doi.org/10.1006/jcis.1999.6372>.

Milici, R.C., Swezey, C.S., 2006. Assessment of Appalachian Basin Oil and Gas Resources: Devonian Shale–Middle and Upper Paleozoic Total Petroleum System. techreport. U.S. Geological Survey. <https://pubs.usgs.gov/of/2006/1237/of2006-1237.pdf> accessed January 2018.

Morsy, S., Sheng, J. J. and Hetherington, C.J., Soliman, M.Y., Ezewu, R.O., 2013. Impact of matrix acidizing on shale formations, Society of Petroleum Engineers. Society of Petroleum Engineers. doi:[10.2118/167568-MS](https://doi.org/10.2118/167568-MS).

Mullen, J., 2010. Petrophysical characterization of the eagle ford shale in south texas, Society of Petroleum Engineers. Society of Petroleum Engineers. doi:[10.2118/138145-MS](https://doi.org/10.2118/138145-MS).

Murphy, E.E., Praznik, G., Quirein, J., Galford, J.E., Witkowsky, J.M., Chen, S., 2013. A workflow to evaluate mineralogy, porosity, toc, and hydrocarbon volume in the eagle ford shale, Society of Petroleum Engineers. Society of Petroleum Engineers. doi:[10.2118/167012-MS](https://doi.org/10.2118/167012-MS).

Niu, C., Hao, Y.z., Li, D.I., Lu, D.t., 2014. Second-Order Gas-Permeability Correlation of Shale During Slip Flow. SPE Journal 19, 786–792. URL: <https://doi.org/10.2118/168226-PA>, doi:[10.2118/168226-PA](https://doi.org/10.2118/168226-PA), arXiv:<https://onepetro.org/SJ/article-pdf/19/05/786/2100934/spe-168226-pa.pdf>.

Pritchard, P.J., Leylegian, J.C., 2010. Introduction to fluid mechanics. 8th ed., John Wiley and Sons, INC.

Rezaee, R., 2015. Fundamentals of gas shale reservoirs. John Wiley & Sons.

Ridgley, J.L., Condon, S.M., Hatch, J.R., 2013. Geology and oil and gas assessment of the mancos-menefee composite total petroleum system, U.S. Geological Survey, San Juan Basin, New Mexico and Colorado. Digital Data Series 69-F. chapter 4, pp. 1–97.

Rocha, R.P.A., Cruz, M.E., 2010. Calculation of the permeability and apparent permeability of three-dimensional porous media. Transport in Porous Media 83, 349–373. URL: <https://doi.org/10.1007/s11242-009-9445-7>, doi:[10.1007/s11242-009-9445-7](https://doi.org/10.1007/s11242-009-9445-7).

Sakhaee-Pour, A., Bryant, S.L., 2012. Gas Permeability of

Table 24

Estimates of volume fraction of mineral for the three-dimensional volume of 96 subsamples of Eagle Ford parallel 1.

	Layer 1	Layer 2	Layer 3	Layer 4	Layer 5	Layer 6
R1N1	6.87	4.76	1.95	0.42	0.20	0.14
R1N2	0.94	0.48	0.18	0.10	5.6E-02	6.2E-02
R1N3	0.83	0.36	0.20	0.13	9.0E-02	4.4E-02
R1N4	3.44	1.63	1.25	0.46	0.19	9.2E-02
R2N1	1.84	0.74	0.64	0.21	6.7E-02	3.4E-02
R2N2	0.25	0.14	7.1E-02	7.2E-02	3.2E-02	2.9E-02
R2N3	0.18	0.13	7.2E-02	7.4E-02	6.9E-02	4.3E-02
R2N4	0.99	0.72	0.23	0.16	0.10	3.8E-02
R3N1	0.91	0.69	0.27	9.2E-02	8.7E-02	5.0E-02
R3N2	0.37	0.16	0.29	7.3E-02	5.7E-02	2.4E-02
R3N3	0.26	0.2	0.10	7.7E-02	3.1E-02	6.5E-02
R3N4	2.0	0.86	0.22	6.9E-02	7.2E-02	6.5E-02
R4N1	4.44	3.03	1.27	0.32	0.10	7.5E-02
R4N2	0.93	0.44	0.17	1.0E-01	6.6E-02	0.12
R4N3	1.42	0.63	0.36	0.11	5.4E-02	4.7E-02
R4N4	1.36	0.58	0.17	0.11	7.8E-02	4.4E-02
Average volume fraction = 0.573 %						

Table 25

Estimates of volume fraction of mineral for the three-dimensional volume of 96 subsamples of Eagle Ford perpendicular 1.

	Layer 1	Layer 2	Layer 3	Layer 4	Layer 5	Layer 6
R1N1	0	0	3.5E-03	0	0	0
R1N2	0	0	0	0	0	0
R1N3	0	0	0	0	2.3E-02	5.0E-02
R1N4	0	0	0.35	0	8.3E-04	0
R2N1	0	0	2.3E-02	0	0	0
R2N2	0	0	2.1E-02	0	0	0
R2N3	0	0	0	0	0	0
R2N4	0	2.8E-02	2.4	0	0	0
R3N1	0	0	0.26	0	0	0
R3N2	6.1E-03	0	0.17	0	0	0
R3N3	2.5E-03	0	0	0	0	0
R3N4	0	0	8.9E-02	0	0	0
R4N1	0	0	1.2E-03	0	0	0
R4N2	0	0	0	0	0	0
R4N3	0	0	0.12	0	0	0
R4N4	0	0	0	1.9E-02	0	0
Average volume fraction = 0.037 %						

Table 26

Estimates of volume fraction of mineral for the three-dimensional volume of 96 subsamples of Mancos parallel 2.

	Layer 1	Layer 2	Layer 3	Layer 4	Layer 5	Layer 6
R1N1	0.1	0.21	0.19	0.18	0.12	0.10
R1N2	0.1	0.14	6.1E-02	0.18	0.11	0.12
R1N3	0.1	6.6E-02	6.2E-02	6.1E-02	4.8E-02	0.10
R1N4	9.6E-02	0.19	9.1E-02	7.3E-02	6.6E-02	0.12
R2N1	0.1	0.14	0.18	0.94	0.50	0.19
R2N2	0.2	0.17	0.11	5.9E-02	9.8E-02	0.18
R2N3	9.2E-02	5.6E-02	7.7E-02	2.5E-02	0.12	0.30
R2N4	4.4E-02	5.0E-02	6.2E-02	0.11	8.1E-02	0.68
R3N1	0.2	0.20	0.18	0.18	0.19	0.20
R3N2	9.2E-02	6.0E-02	0.11	0.10	8.1E-02	9.5E-02
R3N3	8.8E-02	8.7E-02	0.15	7.1E-02	3.8E-02	0.19
R3N4	7.9E-02	1.0E-01	6.7E-02	5.3E-02	0.15	3.4E-02
R4N1	0.22	0.28	0.24	0.11	0.13	0.19
R4N2	0.16	0.23	0.16	0.13	0.20	0.24
R4N3	9.5E-02	0.14	0.16	0.11	0.19	0.15
R4N4	0.11	0.11	0.13	0.23	0.22	7.9E-02
Average volume fraction = 0.15 %						

Table 27

Estimates of volume fraction of minerals for the three-dimensional volume of 96 subsamples of Mancos perpendicular 1.

	Layer 1	Layer 2	Layer 3	Layer 4	Layer 5	Layer 6
R1N1	0.22	0.98	0.10	8.0E-02	0.14	8.9E-02
R1N2	0.14	8.7E-02	5.3E-02	6.6E-02	5.1E-02	0.12
R1N3	0.17	0.12	5.7E-02	3.7E-02	5.0E-02	6.1E-02
R1N4	0.14	0.12	6.4E-02	3.9E-02	5.3E-02	0.11
R2N1	0.12	0.53	7.6E-02	4.2E-02	9.1E-02	3.2E-02
R2N2	8.5E-02	6.1E-02	4.6E-02	5.8E-02	4.0E-02	5.2E-02
R2N3	6.6E-02	8.0E-02	2.7E-02	2.7E-02	5.2E-02	4.9E-02
R2N4	0.11	0.11	2.8E-02	5.8E-02	4.3E-02	4.5E-02
R3N1	0.2	0.14	2.9E-02	2.8E-02	4.3E-02	5.2E-02
R3N2	0.42	0.16	3.3E-02	1.9E-02	8.2E-02	5.0E-02
R3N3	0.23	7.1E-02	1.3E-02	1.9E-02	8.5E-02	3.8E-02
R3N4	0.23	0.28	6.0E-02	4.4E-02	5.8E-02	6.4E-02
R4N1	0.21	0.19	5.4E-02	6.4E-02	0.13	0.14
R4N2	0.62	0.12	5.8E-02	3.1E-02	7.1E-02	6.7E-02
R4N3	0.34	8.6E-02	3.9E-02	4.9E-02	7.7E-02	0.14
R4N4	0.15	0.10	3.9E-02	4.4E-02	6.5E-02	0.11
Average volume fraction = 0.11 %						

Shale. SPE Reservoir Evaluation Engineering 15, 401–409. URL: <https://doi.org/10.2118/146944-PA>, doi:10.2118/146944-PA, arXiv:<https://onepetro.org/REE/article-pdf/15/04/401/2138832/spe-146944-pa>.

Saraji, S., Piri, M., 2015. The representative sample size in shale oil rocks and nano-scale characterization of transport properties. International Journal of Coal Geology 146, 42 – 54. URL: <http://www.sciencedirect.com/science/article/pii/S0166516215000919>, doi:<https://doi.org/10.1016/j.coal.2015.04.005>.

Shabro, V., Kelly, S., Torres-Verdin, C., Sepehrnoori, K., Revil, A., 2014. Pore-scale modeling of electrical resistivity and permeability in fib-sem images of organic mudrock. GEOPHYSICS 79, 289–299. doi:10.1190/GEO2014-0141.1.

Shao, N., Salman, W., Gavrilidis, A., Angeli, P., 2008. Cfd simulations of the effect of inlet conditions on taylor flow formation. International Journal of Heat and Fluid Flow 29, 1603 – 1611. URL: <http://www.sciencedirect.com/science/article/pii/S0142727X08001161>, doi:<https://doi.org/10.1016/j.ijheatfluidflow.2008.06.010>.

Smith, I.M., Griffiths, D.V., Margetts, L., 2013. Programming the Finite Element Method. Wiley Series in Computational Mechanics Series, Wiley. URL: <https://books.google.co.uk/books?id=ZbtiAAAAQBAJ>.

Stüben, K., 2001. A review of algebraic multigrid. Journal of Computational and Applied Mathematics 128, 281 – 309. URL: <http://www.sciencedirect.com/science/article/pii/S0377042700005161>, doi:<https://doi.org/10.1016/S0377042700005161>.

[//doi.org/10.1016/S0377-0427\(00\)00516-1](https://doi.org/10.1016/S0377-0427(00)00516-1). numerical Analysis 2000. Vol. VII: Partial Differential Equations.

Tao, L., Min, L., Xueqi, J., Wenlian, X., Qingwu, C., 2019. Influence mechanism of pore-scale anisotropy and pore distribution heterogeneity on permeability of porous media. Petroleum Exploration and Development 46, 594 – 604. URL: <http://www.sciencedirect.com/science/article/pii/S187638041960039X>, doi:[https://doi.org/10.1016/S1876-3804\(19\)60039-X](https://doi.org/10.1016/S1876-3804(19)60039-X).

Tarik, S., Qingyang, L., Alan, R.B., Branko, B., B., M.J., 2017. Multi-scale multi-dimensional microstructure imaging of oil shale pyrolysis using x-ray micro-tomography, automated ultra-high resolution sem, maps mineralogy and fib-sem. Applied Energy 202, 628 – 647. URL: <http://www.sciencedirect.com/science/article/pii/S0306261917305512>, doi:<https://doi.org/10.1016/j.apenergy.2017.05.039>.

Tiab, D., Donaldson, E.C., 2004. Petrophysics: theory and practice of measuring reservoir rock and fluid transport properties. Elsevier.

Tinni, A., Fathi, E., Agarwal, R., Sondergeld, C.H., Akkutlu, I.Y., Rai, C.S., 2012. Shale permeability measurements on plugs and crushed samples, Society of Petroleum Engineers. Society of Petroleum Engineers. doi:10.2118/162235-MS.

Tiwari, P., Deo, M., Lin, C.L., Miller, J.D., 2013. Characterization of oil shale pore structure before and after pyrolysis by using x-ray micro ct. Fuel 107, 547 – 554. URL: <http://www.sciencedirect.com/science/article/pii/S0016236113000148>, doi:<https://doi.org/10.1016/S0016236113000148>.

Table 28

Estimates of volume fraction of minerals for the three-dimensional volume of 96 subsamples of Marcellus parallel 2.

	Layer 1	Layer 2	Layer 3	Layer 4	Layer 5	Layer 6
R1N1	0	2.0E-03	0	0	0	0
R1N2	1.2E-02	6.0E-03	0	0	0	2.7E-03
R1N3	3.9E-04	4.4E-03	2.6E-02	0	1.2E-02	1.2E-02
R1N4	5.1E-02	1.1E-02	4.3E-02	5.6E-02	8.1E-03	6.6E-03
R2N1	0	0	1.1E-03	0	0	6.3E-03
R2N2	2.9E-03	0	5.5E-03	7.5E-03	0	0
R2N3	8.3E-03	0	1.8E-02	1.7E-03	1.6E-02	0
R2N4	1.1E-02	2.2E-02	5.1E-03	0	1.6E-02	7.2E-03
R3N1	0	0	0	0	0	0
R3N2	0	1.2E-03	8.9E-04	9.2E-03	0	3.0E-03
R3N3	9.0E-03	5.7E-03	6.4E-03	9.2E-03	0	0
R3N4	3.0E-03	6.8E-02	8.3E-04	4.1E-03	8.3E-04	5.0E-03
R4N1	0	0	0	0	1.5E-03	0
R4N2	0	1.1E-02	5.1E-03	0	5.6E-04	2.1E-03
R4N3	6.8E-03	0	0	1.0E-03	0	2.9E-03
R4N4	6.3E-03	4.8E-03	3.5E-03	1.3E-02	6.2E-02	0

Average volume fraction = 0.007 %

Table 29

Estimates of volume fraction of mineral for the three-dimensional volume of 96 subsamples of Marcellus perpendicular 2.

	Layer 1	Layer 2	Layer 3	Layer 4	Layer 5	Layer 6
R1N1	0.67	0.87	0.21	8.5E-02	4.4E-02	8.6E-03
R1N2	3.5E-02	7.6E-03	1.8E-02	4.4E-02	0.2	0.58
R1N3	0.13	2.6E-02	0.13	0.11	0.12	1.0
R1N4	0.32	1.21	3.1E-02	8.6E-02	5.4E-02	1.4E-03
R2N1	5.9E-02	9.0E-03	1.6E-02	8.1E-02	0.6	6.8E-02
R2N2	8.2E-02	8.4E-02	1.9E-02	0.12	1.16	0.43
R2N3	8.7E-02	4.1E-02	7.1E-03	8.0E-02	5.4E-02	2.4E-04
R2N4	5.5E-03	1.0E-03	0	6.7E-02	5.9E-02	0
R3N1	0.11	0.36	7.8E-03	3.4E-02	8.9E-04	2.7E-03
R3N2	0.93	1.4E-03	3.9E-02	6.6E-02	4.8E-02	1.7E-02
R3N3	1.4E-02	5.6E-04	0	4.8E-02	2.7E-02	8.3E-04
R3N4	1.7E-02	2.1E-03	4.0E-03	2.0E-02	8.3E-03	0
R4N1	0.47	0.19	5.2E-02	3.1E-02	0	3.1E-03
R4N2	6.9E-03	8.2E-03	1.3E-02	5.1E-02	1.0E-02	2.2E-02
R4N3	4.6E-03	0.13	0.12	4.9E-02	1.8E-02	3.3E-02
R4N4	2.3E-02	8.6E-02	8.8E-02	0.11	2.2E-02	1.4E-02

Average volume fraction = 0.13 %

Table 30

Numerical computation of porosity results from Eagle Ford perpendicular 1 subsample L3R2N4 (Table 11). NOTE: n/a means the sample was not considered for simulation.

	N1	N2	N3	N4
R1	n/a	n/a	n/a	n/a
R2	n/a	n/a	n/a	n/a
				57.6
				66.8
R3	n/a	n/a	n/a	n/a
				30.5
				52.3
R4	n/a	n/a	n/a	n/a

Table 31

Numerical computation of porosity results from Eagle Ford perpendicular 1 subsamples L4R2N4, L4R3N4, and L4R4N4 (Table 14). NOTE: n/a means the sample was not considered for simulation.

	N1	N2	N3	N4
R1	n/a	n/a	n/a	n/a
R2	n/a	n/a	n/a	n/a
				87.9
				47.3
R3	n/a	n/a	n/a	57.7
				61
				n/a
R4	n/a	n/a	n/a	50.8
				n/a
				37.6

Table 32

Numerical computation of porosity results from Mancos perpendicular subsample L3R1N4 (Table 17). NOTE: n/a means the sample was not considered for simulation.

	N1	N2	N3	N4
R1	n/a	n/a	32.1	9.9
R2	n/a	n/a	n/a	n/a
R3	n/a	n/a	n/a	n/a
R4	n/a	n/a	n/a	n/a

Table 33

Numerical computation of porosity results from Mancos perpendicular subsamples L4R1N2, L4R1N3, L4R2N2, L4R2N3, L4R2N4, L4R3N2, L4R3N4, L4R4N2, L4R4N3, and L4R4N4. NOTE: n/a means the sample was not considered for simulation.

	N1	N2	N3	N4	
R1	n/a	39.9	n/a	12.7	25.7
		n/a	n/a	n/a	n/a
		n/a	n/a	n/a	n/a
		n/a	n/a	n/a	n/a
R2	n/a	27	26.7	18.2	29.9
		29	33.7	42.3	20.2
		n/a	n/a	n/a	n/a
		n/a	n/a	n/a	n/a
R3	n/a	32	25.4	n/a	34.63
		56.2	32		47
		n/a	n/a		n/a
		n/a	n/a		n/a
R4	n/a	31	26.9	37.17	n/a
		n/a	n/a	n/a	n/a
		n/a	n/a	n/a	n/a
		n/a	n/a	n/a	n/a

j.fuel.2013.01.006.

Torsaeter, M., Vullum, P.E., Nes, O.M., 2012. Nanostructure vs. macroscopic properties of mancos shale, Society of Petroleum Engineers. Society of Petroleum Engineers. doi:doi:10.2118/162737-MS.

Tutuncu, A.N., 2012. The role of mechanical, acoustic and permeability anisotropies on reservoir characterization and field development for two north american fractured unconventional shale reservoirs.

Wang, Z., Jin, X., Wang, X., Sun, L.L., Wang, M., 2016. Pore-scale geometry effects on gas permeability in shale.

Yang, P., Wen, Z., Dou, R., Liu, X., 2017. Permeability in multi-sized structures of random packed porous media using three-dimensional

lattice boltzmann method. International Journal of Heat and Mass Transfer 106, 1368 – 1375. URL: <http://www.sciencedirect.com/science/article/pii/S0017931016319184>, doi:<https://doi.org/10.1016/j.ijheatmasstransfer.2016.10.124>.

Zhang, J., Lai, B., Liu, H.H., Li, H., Georgi, D., 2016. Textural and mineralogical control on tensile strength of eagle ford and manco shales samples, Unconventional Resources Technology Conference. Society of Petroleum Engineer.

Zhang, L., Li, D., Lu, D., Zhang, T., 2015. A new formulation of apparent permeability for gas transport in shale. Journal of Natural Gas Science and Engineering 23, 221–226. URL: <https://www.sciencedirect.com/science/article/pii/S1875510015000554>, doi:<https://doi.org/10.1016/j.jngse.2015.01.042>.

Zhang, S., Sheng, J.J., 2017a. Effect of water imbibition on hydration

Table 34

Numerical computation of permeability (m^2) results from Eagle Ford perpendicular 1 subsample L3R2N4. Corresponding to Table 30. NOTE: n/a means the sample was not considered for simulation.

	N1	N2	N3	N4	
R1	n/a	n/a	n/a	n/a	
R2	n/a	n/a	n/a	n/a	n/a
				3.2E-20	5.8E-20
				n/a	n/a
				1.5E-21	1.9E-19
R3	n/a	n/a	n/a	n/a	
R4	n/a	n/a	n/a	n/a	

Table 35

Numerical computation of permeability (m^2) results from Eagle Ford perpendicular 1 sub-samples L4R2N4, L4R3N4, and L4R4N4. Corresponding to Table 31. NOTE: n/a means the sample was not considered for simulation.

	N1	N2	N3	N4	
R1	n/a	n/a	n/a	n/a	
R2	n/a	n/a	n/a	n/a	n/a
				n/a	3.5E-19
				n/a	n/a
				5.0E-20	7.6E-21
R3	n/a	n/a	n/a	1.1E-19	8.1E-19
				n/a	n/a
				n/a	8.743E-19
				3.264E-19	n/a
R4	n/a	n/a	n/a	n/a	n/a
				3.5E-19	n/a
				n/a	6.2E-19
				5.9E-19	n/a

Table 36

Numerical computation of permeability (m^2) results from Mancos perpendicular subsample L3R1N4. Corresponding to Table 32. NOTE: n/a means the sample was not considered for simulation.

	N1	N2	N3	N4
R1	n/a	n/a	1.934E-20	1.662E-20
			n/a	n/a
R2	n/a	n/a	n/a	n/a
R3	n/a	n/a	n/a	n/a
R4	n/a	n/a	n/a	n/a

Table 37

Numerical computation of permeability (m^2) results from Mancos perpendicular subsamples L4R1N2, L4R1N3, L4R2N2, L4R2N3, L4R2N4, L4R3N2, L4R3N4, L4R4N2, L4R4N3, and L4R4N4. Corresponding to Table 33. NOTE: n/a means the sample was not considered for simulation.

	N1	N2		N3		N4	
R1	n/a	1.332E-19	n/a	4.3E-20	8.5E-18	n/a	
		n/a	n/a	n/a	n/a		
		n/a	n/a	n/a	n/a		
		n/a	n/a	n/a	n/a		
R2	n/a	4.7E-20	5.4E-20	5.6E-21	3.9E-21	1.5E-20	n/a
		7E-20	4.6E-20	1.8E-19	1.9E-19	n/a	n/a
		n/a	n/a	n/a	n/a	n/a	n/a
		n/a	n/a	n/a	n/a	n/a	n/a
R3	n/a	3E-20	3.5E-21	n/a		2.415E-18	1.8E-18
		1.6E-19	3.4E-20			5.1E-19	8.2E-20
		n/a	n/a			n/a	n/a
		n/a	n/a			n/a	n/a
R4	n/a	4.2E-19	4.2E-19	4.7E-20	n/a	7.7E-19	8.7E-19
		n/a	n/a	n/a	n/a	n/a	n/a
		n/a	n/a	n/a	n/a	n/a	n/a
		n/a	n/a	n/a	n/a	n/a	n/a

media. Transport Porous Media .
 Zhu, L., Z.C.Z.C.Z.X.Z.Z.N.X.L.W.Z.B., 2019. Challenges and prospects of digital core-reconstruction research. *Geofluids* 2019, 29. URL: <https://doi.org/10.1155/2019/7814180>, doi:10.1155/2019/7814180.
 Zou, Y., Zhao, X., Chen, Q., 2018. Comparison of star-ccm+ and ansys fluent for simulating indoor airflows. *Building Simulation* 11, 165–174. URL: <https://doi.org/10.1007/s12273-017-0378-8>, doi:10.1007/s12273-017-0378-8.

induced fracture and permeability of shale cores. *Journal of Natural Gas Science and Engineering* 45, 726–737. URL: <https://www.sciencedirect.com/science/article/pii/S1875510017302548>, doi:<https://doi.org/10.1016/j.jngse.2017.06.008>.
 Zhang, S., Sheng, J.J., 2017b. Effects of salinity and confining pressure on hydration-induced fracture propagation and permeability of mancos shale. *Rock Mechanics and Rock Engineering* .
 Zhang, S., Sheng, J.J., Shen, Z., 2017. Effect of hydration on fractures and permeabilities in mancos, eagleford, barnette and marcellus shale cores under compressive stress conditions. *Journal of Petroleum Science and Engineering* 156, 917–926. URL: <https://www.sciencedirect.com/science/article/pii/S092041051630688X>, doi:<https://doi.org/10.1016/j.petrol.2017.06.043>.
 Zhaoli, G., Zhao, T.S., 2002. Lattice boltzmann model for incompressible flows through porous media. *Phys. Rev. E* 66, 036304. URL: <https://link.aps.org/doi/10.1103/PhysRevE.66.036304>, doi:10.1103/PhysRevE.66.036304.
 Zheng, B., Li, J.H., 2015. A new fractal permeability model for porous media based on kozeny-carman equation. *Natural Gas Geoscience* 26, 193–198. doi:10.11764/j.issn.1672-1926.2015.01.0193.
 Zhengwen, Z., Reid, G., 2006. A criterion for non-darcy flow in porous

Declaration of Interest Statement

On behalf of other author, I want to say there is no competing financial interests or personal relationships that could have appeared to influence the work reported in this paper.

Sincerely yours,

Signed

James O. Adeleye, Ph.D.

First Technical University, Ibadan, Nigeria

Tel.: +234 8100946184